Physics of Fluids

RESEARCH ARTICLE | APRIL 10 2025

A computational analysis of flow dynamics and heat transfer in a wavy patterned channel using physics-informed neural networks

Aritra Roy (অরিত্র রায়) ; Ayan Mukherjee (অয়ন মুখার্জি); Balbir Prasad (बलबीर प्रसाद) ; Ameeya Kumar Nayak (अमीय कुमार नायक)

Physics of Fluids 37, 043610 (2025)
https://doi.org/10.1063/5.0264160

Physics of Fluids ARTICLE pubs.aip.org/aip/pof

A computational analysis of flow dynamics and heat transfer in a wavy patterned channel using physics-informed neural networks

Cite as: Phys. Fluids **37**, 043610 (2025); doi: 10.1063/5.0264160
Submitted: 9 February 2025 · Accepted: 27 March 2025 ·
Published Online: 10 April 2025

Aritra Roy (অরিত্র রায়),[1] Ayan Mukherjee (অয়ন মুখার্জি),[2,3] Balbir Prasad (बलबीर प्रसाद),[2] and Ameeya Kumar Nayak (अमीय कुमार नायक)[4,a)]

AFFILIATIONS

[1]Department of Mechanical Engineering, Indian Institute of Technology (Indian School of Mines), Dhanbad 826004, India
[2]Department of Mining Engineering, Indian Institute of Technology (Indian School of Mines), Dhanbad 826004, India
[3]Department of Computer Science and Engineering, Indian Institute of Technology (Indian School of Mines), Dhanbad 826004, India
[4]Department of Mathematics, Indian Institute of Technology, Roorkee 247667, India

[a)]**Author to whom correspondence should be addressed:** ameeyakumar@gmail.com

ABSTRACT

The current study utilizes an unsupervised physics-informed neural network (PINN) that leverages heuristic optimization techniques to solve steady-state incompressible Navier–Stokes and energy equations in wavy channels for varying Reynolds numbers. Further, in asymmetric cases, in-phase and out-phase shifts between upper and lower channel walls are considered to mimic actual physiological structures occurring in many natural and industrial process. Moreover, the energy transfer equation is involved in the flow governing equation to accomplish the mixed convection flow for the fluid volume movement. Streamwise and cross-streamwise velocity components, pressure drop, and wall shear stresses are computed, and heat transfer characteristics are also analyzed. PINN predictions are compared with the conventional computational fluid dynamics results, ensuring excellent accuracy. The higher accuracy is obtained due to a new architecture of the deep learning model that ensures a conservative relationship between the stress and flow variables. Additionally, a novel scheduler algorithm is implemented to achieve convergence faster by updating the learning rate dynamically. Overall, the study demonstrates the capability of PINN (a more computationally feasible framework) for solving fluid dynamics and heat transfer problems and elucidating separation and reattachment flow dynamics in complex corrugated geometries. In uniform and non-uniform temperature distribution, the Nusselt number increases significantly with Reynolds number showing a heat transfer enhancement in corrugated geometries.

I. INTRODUCTION

Flow dynamics of wavy channels are extensively utilized in various engineering applications, primarily for mixing of various components and their enhanced capabilities compared to flat channels and significant role in numerous phenomena, including the generation of wind waves on water, the formation of sedimentary ripples in river channels, the development of dunes in deserts, the stability of liquid films in contact with gas streams, the rippling of melting surfaces, and the transpiration cooling of reentry vehicles and rocket boosters.[1] Additionally, it affects cross-hatching on ablative surfaces and film vaporization in combustion chambers. Physiologists and engineers are also keen on studying this to understand blood and urinary flow,[2] aiming to apply the findings to optimize artificial organs.[3,4] This richness in physical phenomena in a relatively simple geometry motivates scientific community over last few years to investigate the flow dynamics in complex geometries. In this regard, Burns and Parkes[5] addressed viscous flow in channels and pipes with sinusoidal variations, including peristaltic motion, assuming a sufficiently low Reynolds number (Re) for the Stokes approximation to hold, where inertial forces are negligible compared to viscous ones. They solved the problem by representing the stream function as a Fourier cosine series and determined the coefficients by assuming small amplitude values. Sobey[6] conducted numerical studies on steady and unsteady flow through furrowed channels, focusing on the effects of the Re, including cases of separated flow. The concept of multistructured boundary layers developed by Stewartson and Williams[7] provides a relationship between

geometric parameters and the Re for the flow separation. Stephanoff *et al.*[8] later compared Sobey's numerical results with the experimental data from visualization techniques. Hall[9] simulated the unsteady oscillatory viscous flow in pipes and channels of a slowly varying cross section. In addition to the numerical studies, many experimental investigations are also performed to determine the flow patterns in an axisymmetric stenosis, elucidating the Re effect on the flow separation (Young and Tsai[10]). Nishimura *et al.*[11] explored the flow behavior in a channel with symmetric wavy walls, analyzing the pressure drop and wall shear stresses (WSS) variation with Re from laminar to turbulent flow regimes.

The scientific community is perplexed to develop techniques to enhance heat transfer in compact heat exchangers operating under laminar flow conditions.[12] These methods aim to effectively disrupt the boundary layer that develops on the heat exchange surface and replace it with fluid from the core.[13] This process forms a new boundary layer with steeper temperature and concentration gradients near the wall, improving transfer rates. Common approaches include using offset fins, louvers, vortex generators, interconnected channels, acoustic flow excitation,[14] and oscillatory inflow.[15] The primary objective of this study focused on maximizing heat and mass transfer on the flow domain. However, factors, such as design simplicity, manufacturing ease, dust accumulation, maintenance, and scalability, are also critical considerations in selecting the most effective method. One of the simplest methods is to use a wavy patterned channel to enhance heat transfer in the wavy channel. This is easy to fabricate and can provide significant operational efficiency. O'Brien and Sparrow[16] did one of the early pioneering work on studying the heat transfer characteristics in the fully developed region of a periodic channel at various Reynolds numbers. Ali and Ramadhyani[17] conducted extensive experimental study on flow visualization and convective heat transfer in the corrugated passages. Attempts were made by Zhang *et al.*[18] to conduct numerical study to analyze the chaotic flow patterns and heat transfer characteristics caused by a curved wavy channel.

Simulating complex flow features, such as flow separation in wavy channels using conventional numerical methods, becomes challenging because of the time-consuming grid generation and independence process. To cope with these difficulties, many researchers tried to apply deep learning (DL) techniques to possess various advantages for simulation to capture nonlinear effects effectively. These enhanced methodologies are capable of providing accurate solutions to a physical problem. Unlike computational fluid dynamics (CFD) solutions, this does not require grid refinement (for convergence and stability) and grid independent study for the dependent variables to be evaluated in the flow field.[19] The limitations of conventional CFD techniques, such as grid generation and achieving grid independence, can be time-consuming and challenging particularly for complex geometries, which are overcome by the DL techniques for capturing the spatiotemporal relationships in physical systems.[20] The advent of various architectures, such as convolutional neural networks (CNNs)[21] and long short-term memory networks (LSTM),[22] has paved the way for the creation of models based on deep learning (DL)[23] capable of simulating intricate physical systems while capturing spatiotemporal relationships in predictions. DL offers highly effective modeling techniques for data-intensive fields such as computer vision, natural language processing, and speech recognition. However, creating interpretable and generalizable models remains a challenge, especially in the areas where data are scarce, such as in complex physical flow systems.[24] Purely data-driven DL methods require large amounts of data for training, which may not always be available for many scientific applications. Moreover, these models often fail to incorporate physical constraints, potentially resulting in excellent fits to observational data while neglecting the fundamental physical laws. To address this issue, combining the laws of the governing physical environment and the expertise of the domain into the training process can lead to more accurate and reliable models. This domain knowledge can be informative, guiding the model toward a more profound physical or mathematical understanding of the system alongside observational data, which remains the basis of physics-informed neural networks (PINNs).[25]

Physics-informed neural networks (PINNs), first proposed by Raissi *et al.*,[26] are deep learning frameworks that implement both data and physical laws, expressed through governing partial differential equations (PDEs), into the learning process. This simple yet powerful construction allows us to tackle a wide range of problems in computational science. PINNs have proven to be highly effective in solving both forward and inverse problems across a wide range of PDE-related applications.[27] It uses a fully connected deep neural network (DNN) [also known as multilayer perceptrons (MLPs)] based on optimization problems or residual loss functions to solve a PDE. Moreover, a number of new variants of PINNs have also been proposed by the research community in the recent times, including various domain-decomposition based PINNs, such as cPINN (conservative PINN),[28] xPINN (extended PINN),[29] hp-variational PINN (hp-VPINN),[30] and deep-domain decomposition method.[31] These recent advances of the scientific machine learning community have taken immense interest in solving various fluid flow applications, such as super-resolution and diagnosis of 4D-flow magnetic resonance imaging (MRI)[32] and prediction of near-wall blood flow from sparse data.[33] Laubscher and Rousseau[34] used PINNs to predict laminar incompressible flow and heat transfer over two heated cylinders subjected to constant wall temperature heating. Similar to Rao *et al.*,[35] they have used diffusion heat flux as an output variable in addition to temperature. They found that the error between CFD and PINN results was immensely accurate for velocity, pressure, and temperature fields, respectively. PINNs have shown its reliability and accuracy not only in the laminar flow regime but also useful in predicting the turbulent flow behavior. Eivazi *et al.*[36] studied four different two-dimensional incompressible turbulent flow cases using Reynolds-averaged Navier–Stokes (RANS) equations and observed the effects of zero-pressure gradient boundary layer, adverse pressure gradient boundary layer, and turbulent flows over a NACA-4412 airfoil and a periodic hill. Xiao *et al.*[37] performed RANS modeling for Rayleigh–Taylor turbulent mixing using PINNs. Moreover Parish and Duraisamy[38] and Li *et al.*[39] went on to perform large eddy simulation (LES) of an isotropic homogeneous periodic turbulence in a box resolving the energy spectrum. A detailed discussion on the prevailing trends in the embedding of physics in machine learning algorithms and the diverse applications of PINNs can be found in the work of Karniadakis *et al.*,[25] where they reviewed the applications of embedding physics into machine learning for simulating both forward and inverse multiphysics problems.

Despite numerous advancements, a dearth of studies investigate the flow dynamics inside wavy channels using PINNs. Shah and Anand[40] did insightful research on periodic flow in wavy corrugated channels using PINNs, demonstrating the precision of PINN

compared to CFD results. However, a research gap exists in the literature on the application of PINN to solve aperiodic flows with conventional boundary conditions used in CFD. Also, flow dynamics in asymmetric wavy channels mimicking realistic blood vessels has not been investigated using PINN to date. Bridging these research gaps, the current study explores the use of PINN for the solution of aperiodic flows in symmetric and asymmetric wavy channels for varying Re and other modulation parameters. The asymmetricity in the wavy channels is incorporated by applying positive and negative phase shifts between the upper and lower wavy channel walls. Streamwise and cross-streamwise velocity components and WSS are computed using PINN and compared with CFD results. Moreover, flow reversal due to recirculation zones in asymmetric wavy channels is adequately captured and highlighted. Additionally, we also studied the heat transfer characteristics of symmetric channel with uniform and non-uniform temperature distribution on the wavy walls along with its effects on Nusselt number variation across the channel and the subsequent enhancement of heat transfer properties. We have also used a loss-based learning rate scheduler to dynamically adjust the learning rate while training. This enhances the entire DL model to accelerate convergence for the solution of the governing equation of the physical system.

This paper deals with a conservative approach that uses constitutive Cauchy stress formulations and reduces the order of derivatives in the governing PDE. As a result, the mean squared error (MSE) is significantly reduced from the previous study of Shah and Anand.[40] We have also created a learning rate scheduler algorithm. Though quite widely used in the deep learning community, this sub-routine written in Python 3.10.14 and PyTorch 2.4 is based on the MSE loss encountered in each training epoch. This scheduler algorithm monitors the mean squared error obtained by putting the values obtained by PINNs in the governing PDE equations. If the mean squared error does not decrease much, the learning rate is decreased. This allows the PDE to reach convergence faster with a lesser number of training epochs than previous studies. Further intricacies of flow separation and recirculation in asymmetrical regions, owing to zero wall shear stress regions, have also been widely analyzed and discussed. This is of particular importance to show the well mixing of fluids and enhanced heat transfer effects. This article is organized as follows: Sec. I outlines the motivation for the work and presents systematic literature review and literature gap. Section II introduces the mathematical model required for the numerical computation of hydrodynamics and thermal effects inside the wavy channel. Section III details the framework of the procedure adopted for the numerical computation of flow features and heat transfer. Section IV validates the present DNN architecture against benchmark problems solved using CFD. Section V discusses comprehensively the results obtained from numerical simulation along with validation from the corresponding works previously done in the literature. Finally, Sec. VI encapsulates the conclusive insight of this study, highlighting the key findings along with their physical implications, and envisions the potential scope for future improvements.

II. FLOW CONFIGURATION AND GOVERNING EQUATIONS

Literature suggests that the flow separation and optimized heat transfer is possible by considering a modulated geometry. This study implements a conservative deep learning algorithm to analyze the flow phenomenon in both symmetric and asymmetric wavy patterned channels. Our study is restricted to analyzing the heat transfer

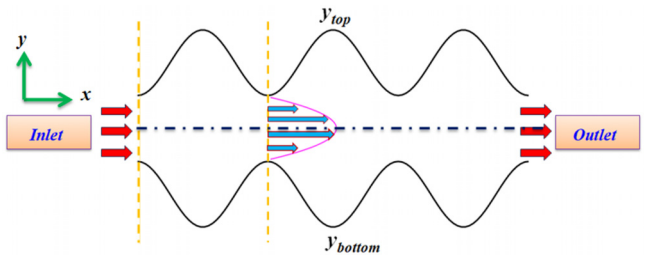

FIG. 1. Schematic diagram of the 2D flow geometry.

characteristics for a symmetric channel with uniform and non-uniform thermal boundary conditions. An infinitely long approximation is invoked for the flow variables in the z-direction compared to the x-y plane, thus reducing the dimensionality of the problem. From an extended physical domain as shown in Fig. 1, we have tried to analyze at the extremities of the domain to capture the intricacies of flow dynamics caused by boundary layer effects.

A. Description of the physical system

The symmetric wavy wall structure along x-axis is taken as a superimposition of two sinusoidal waves:

$$y_{\text{top}} = a\sin\left(Bx + \frac{\pi}{2}\right) + \left(\frac{H_{\min}}{2} + a\right), \tag{1}$$

$$y_{\text{bottom}} = a\sin\left(Bx + \frac{\pi}{2} + \phi\right) - \left(\frac{H_{\min}}{2} + a\right). \tag{2}$$

Here, Eqs. (1) and (2) represent the spatial variation of y-coordinates for the upper and lower boundaries, respectively. The length of each periodic module is specified as $L = 8$. In Eqs. (1) and (2), $B = \frac{2\pi}{L}$ denotes the wave number for the periodic module. For this study, a module length ratio of $L/a = 8$ and a height ratio of $\frac{H_{\min}}{H_{\max}} = 0.3$ were selected, with the amplitude a set to 1. Notably, an additional parameter in Eq. (2), ϕ, incorporates the asymmetry in the wavy module. To break the symmetry in the system, ϕ can be either positive or negative depending on whether we want the phase shift to be in phase or out of phase. As shown in Fig. 2, $H_{\min}$ is the smallest channel height, located at the inlet and outlet of each

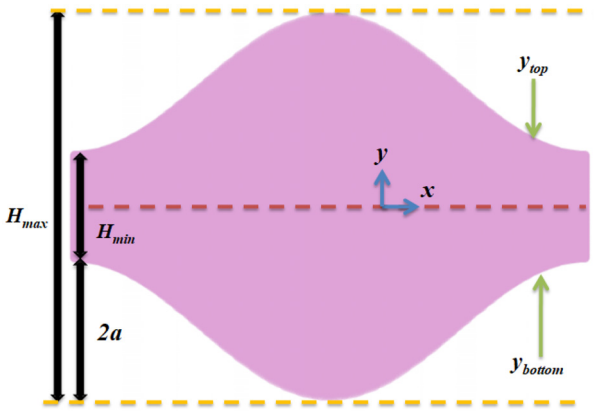

FIG. 2. Computational domain with symmetrical wavy side-walls.

module, while H_{max} is the maximum channel height at the module's center. The Reynolds number for this configuration is defined as

$$Re = \frac{\rho u_{avg} H_{avg}}{\mu}, \tag{3}$$

where

$$u_{avg} = \text{mean characteristic velocity in a single module}, \tag{4}$$

$$H_{avg} = \text{average height} = \frac{H_{min} + H_{max}}{2}. \tag{5}$$

In these expressions, H_{avg} provides an effective height for calculating average flow parameters.

B. Governing equations of hydrodynamics and energy equation

In this study, a two-dimensional steady and incompressible fluid flow in a wavy pattern channel is considered. The flow governing equation deals with the conservation of mass, momentum in the following continuum, and constitutive formulations, given by

$$\nabla^* \cdot \mathbf{v}^* = 0, \tag{6}$$

$$(\mathbf{v}^* \cdot \nabla^*)\mathbf{v}^* = \frac{1}{\rho}\nabla^* \cdot \boldsymbol{\sigma}^*, \tag{7}$$

$$\boldsymbol{\sigma}^* = -p^*\mathbf{I} + \mu(\nabla^*\mathbf{v}^* + \nabla^*\mathbf{v}^{*\top}), \tag{8}$$

where $\boldsymbol{u}^*$, μ, ρ, $\boldsymbol{\sigma}^*$, and $p^* = -\text{tr}\,\boldsymbol{\sigma}^*/2$ designates the velocity field, dynamic viscosity, density, Cauchy stress tensor, and mechanical pressure, respectively. The advantages of using the continuum-mechanics-based formulation are listed as follows:

1. It reduces the order of derivatives when a mixed-variable scheme in physics-informed neural networks (PINNs) is applied.
2. It improves the trainability of deep neural networks (DNNs), as evidenced by the comparison of numerical results.

In addition to the hydrodynamics, the background flow has been used to analyze the convective heat transfer inside the wavy channel using a steady-state two-dimensional energy equation assuming no heat dissipation. The corresponding governing equation is

$$u^*\frac{\partial T^*}{\partial x^*} + v^*\frac{\partial T^*}{\partial y^*} = \frac{k}{\rho C_p}\nabla^*(\nabla^* T^*), \tag{9}$$

where T^*, α, ρ, and C_p denote the scalar temperature field, thermal diffusivity, fluid density, and specific heat capacity at constant pressure, respectively. Equations (6)–(8) are non-dimensionalized by their scalar characteristic length and velocity scales given by

$$\mathbf{x} = \frac{\mathbf{x}^*}{H_{avg}}, \quad \nabla = H_{avg}\nabla^*, \quad Re = \frac{\rho u^*_{avg} H_{avg}}{\mu},$$
$$Pr = \frac{\mu C_p}{k}, \quad p = \frac{p^* H_{avg}}{\mu u^*_{avg}}, \quad \theta = \frac{T^* - T_w}{T_{ref} - T_w},$$

where Pr, θ^*, T_w, and T_{ref} represent the Prandtl number, non-dimensionalized temperature, wall temperature, and reference temperature, respectively. The above-mentioned non-dimensionalized variables are incorporated into Eqs. (6)–(8) to obtain the following equations:

$$\frac{\partial u}{\partial x} + \frac{\partial v}{\partial y} = 0, \tag{10}$$

$$u\frac{\partial u}{\partial x} + v\frac{\partial u}{\partial y} = \frac{\partial \sigma_{xx}}{\partial x} + \frac{\partial \sigma_{xy}}{\partial y}, \tag{11}$$

$$u\frac{\partial v}{\partial x} + v\frac{\partial v}{\partial y} = \frac{\partial \sigma_{yx}}{\partial x} + \frac{\partial \sigma_{yy}}{\partial y}, \tag{12}$$

$$u\frac{\partial \theta}{\partial x} + v\frac{\partial \theta}{\partial y} = \frac{1}{\text{Re}\cdot\text{Pr}}\nabla^2\theta. \tag{13}$$

The above-mentioned equation has been instrumental in evaluating the loss function of DNN, which has been solved as a minimization problem. In order to solve the aforementioned PDEs [Eqs. (10)–(12)], a mixed-variable approach is used. In this setup, deep neural networks map the spatiotemporal variables $\{\mathbf{x}\}^T$ to the mixed-variable solution $\{\psi, p, \boldsymbol{\sigma}\}$, where ψ is the stream function that has been used instead of the velocity $\mathbf{v}$ to ensure the divergence-free condition of the flow. In a two-dimensional scenario, the velocity components can be evaluated from the stream function ψ as follows:

$$u = \frac{\partial \psi}{\partial y}$$
$$v = -\frac{\partial \psi}{\partial x}.$$

In order to make the system of PDEs—Eqs. (10)–(13), a well-posed problem, a set of well-defined boundary conditions need to be prescribed, as depicted in Fig. 3. For the hydrodynamic problem, a constant mass flow rate and temperature is given at the inlet. At the walls, a no-slip boundary condition for the velocity field along with $\theta = 0$ is given for the temperature field. Finally, at the exit of the wavy channel, a fully developed temperature profile and velocity profile (zero-pressure exit condition) is prescribed.

III. MATHEMATICAL MODEL

In this section, we present the methodological foundation of physics-informed neural networks (PINNs) and their use in finding solution to partial differential equations (PDEs). The primary objective of PINNs is to embed the knowledge of governing physical laws, expressed as PDEs, directly into the training of a deep neural network, enabling the network to approximate the solution effectively. A PINN model is composed of multiple layer perceptron (MLP) that maps the

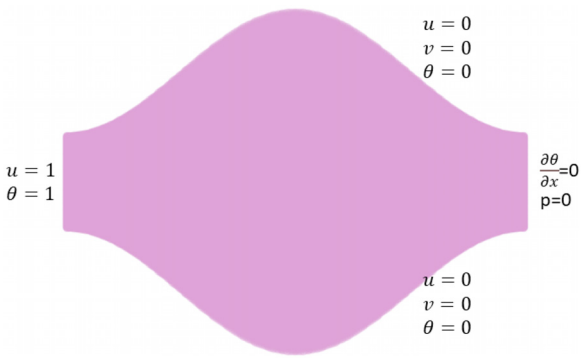

FIG. 3. Hydrodynamic and thermal boundary conditions along the channel wall.

spatiotemporal coordinates to the solution. An auxiliary residual network computes the residual of the governing equations. Thus, we can directly tackle nonlinear problems without any prior assumptions, linearization, local time-stepping, or grid dependence issue of variables to be computed.

A. Mathematical framework of PINNs

Deep neural networks (DNNs) have been proven to be universal approximators for continuous functions,[41] consisting of multiple levels (referred to as layers). Each layer is made up of neurons or nodes. Through the application of a series of nonlinear transformations, called activation functions, and training on sufficiently large datasets, DNNs are capable of learning highly complex functions utilizing the backpropagation algorithm. A fundamental form of neural networks is the multilayer perceptron (MLP), also called fully connected networks, which consist of two or more layers in which each node is connected to every node in both the previous and subsequent layers.[42] To compute the unknowns of Eqs. (10)–(12), let $u(x,y)$, $v(x,y)$ and $p(x,y)$ denote the axial and transverse scalar components of velocity and pressure, respectively, where $\mathbf{x} \in \mathbb{R}^2$ represents the spatial coordinate. PINNs approximate the spatial solutions by using a neural network (FNN), given by

$$(u, v, p) = F_{NN}(x, y, \Theta),$$

where (x,y) and (u,v,p) denote the inputs and outputs of the neural network, respectively, and Θ denotes the training parameters. For the fully connected network (see Fig. 4), Θ includes the weights and biases of multiple hidden layers. For the hidden layer k, the relationship between the output vector Y_k and the input vector X_k can be simply expressed as

$$Y_k = \phi(W_k X_k + b_k),$$

where W_k and b_k are weights and biases and $\phi(\cdot)$ denotes the activation function, which is used to represent the non-linearity of the solutions. We use the hyperbolic tangent function, namely, $\phi(\cdot) = \tanh(\cdot)$, throughout the paper unless otherwise stated. In this context, solving the nonlinear system of the governing equations is equivalent to learning the weights and biases of the network. However, for a multilayer perceptron problem, this can be defined as

$$Y_k = \phi_k(Y_{k-1} X_k + b_k). \tag{14}$$

The weights and biases in Eq. (14) are updated using the backpropagation mechanism[43] to minimize the value of the loss functional ($\mathcal{L}$), ideally driving it toward zero. This process is framed as an optimization problem, where various optimization algorithms (optimizers) are employed to iteratively adjust the weights and biases $\left(\frac{\partial \mathcal{L}}{\partial W_i}\right)$. To compute the necessary derivatives, the neural network leverages automatic differentiation (AD), which automatically calculates the gradients of the loss function with respect to the network's parameters, facilitating the update process. In this work, we have used PyTorch (2.4.1)[44] for creating the neural network. The architecture of the proposed PINN for fluid dynamics simulation is presented in Fig. 4. It is quite evident that the neural network comprises of two spatial variables as input and five direct outputs, namely, ψ, p, and σ. The derived outputs from the output layer of the multilayer perceptrons (MLPs) are u, v, p, and σ.

The general form of a PDE can be written as

$$u_t + N[u] = 0, \quad x \in \Omega, \quad t \in [0, T],$$

where $u(x,t)$ is the solution to the equation, N represents a linear or nonlinear differential operator, and Ω is a subset of the n dimensional space $\mathbb{R}^n$. The boundary conditions also need to be satisfied along the inlet Γ_i, wall Γ_w, and exit Γ_e to make it a well-posed problem. In the forward problem, the spatial coordinate x and the temporal coordinate

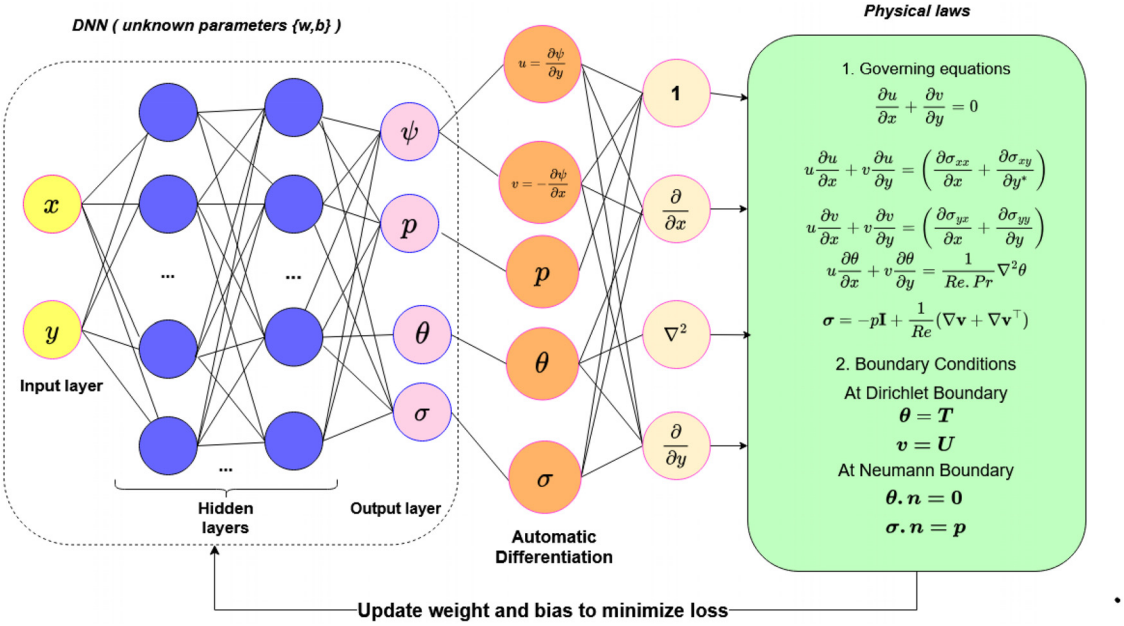

FIG. 4. Deep neural network architecture of PINN.

t are provided as input variables to the neural network, while the solution $u(x,t)$ is the output of the network.

The loss function can be defined by

$$\mathcal{L} := u_t + N[u]. \tag{15}$$

On comparing with Eqs. (10)–(12), we can obtain the loss function similar to Eq. (15) as follows:

$$\mathcal{L}_{g_1} = \frac{1}{N_c}\sum_{i=1}^{N_c}\left|\frac{\partial \hat{u}}{\partial x} + \frac{\partial \hat{v}}{\partial y}\right|^2, \tag{16}$$

$$\mathcal{L}_{g_2} = \frac{1}{N_c}\sum_{i=1}^{N_c}\left|u\frac{\partial u}{\partial x} + v\frac{\partial u}{\partial y} - \left(\frac{\partial \sigma_{xx}}{\partial x} + \frac{\partial \sigma_{xy}}{\partial y}\right)\right|^2, \tag{17}$$

$$\mathcal{L}_{g_3} = \frac{1}{N_c}\sum_{i=1}^{N_c}\left|u\frac{\partial v}{\partial x} + v\frac{\partial v}{\partial y} - \left(\frac{\partial \sigma_{yx}}{\partial x} + \frac{\partial \sigma_{yy}}{\partial y}\right)\right|^2, \tag{18}$$

$$\mathcal{L}_{g_4} = \frac{1}{N_c}\sum_{i=1}^{N_c}\left|u\frac{\partial \theta}{\partial x} + v\frac{\partial \theta}{\partial y} - \frac{1}{\mathrm{Re}\cdot\mathrm{Pr}}\nabla^2\theta\right|^2, \tag{19}$$

$$\mathcal{L}_{g_5} = \frac{1}{N_c}\sum_{i=1}^{N_c}\left|\sigma + p\mathbf{I} - \frac{1}{Re}(\nabla\mathbf{v} + \nabla\mathbf{v}^\top)\right|^2. \tag{20}$$

Similar to Eq. (15), the corresponding boundary losses need to be defined along the inlet boundary Γ_i, wall boundary Γ_w, and exit boundary Γ_e. In the same manner, $\mathcal{L}_{g_1}$, $\mathcal{L}_{g_2}$, $\mathcal{L}_{g_3}$, $\mathcal{L}_{g_4}$, and $\mathcal{L}_{g_5}$ denote the physics loss occurring the system due to the governing equation. All the loss functions are evaluated in Eqs. (16)–(20), wherein N_c represents the number of collocation points inside the bulk of the domain. The computational domain to calculate the losses is depicted in Fig. 5.

Hence, the net loss due to the domain collocation points is the scalar sum of all the losses,

$$\mathcal{L}_g = \mathcal{L}_{g_1} + \mathcal{L}_{g_2} + \mathcal{L}_{g_3} + \mathcal{L}_{g_4} + \mathcal{L}_{g_5}. \tag{21}$$

Similarly, we have the physics loss occurring due to the boundary conditions along the boundaries Γ of the domain. The boundary losses can be classified into two broad categories, namely, Dirichlet and Neumann boundary conditions. Let us consider that we have N_d number of boundary points with Dirichlet boundary conditions and N_n number of points with Neumann boundary conditions, respectively. Subject to the adaptability of the problem with various boundary conditions, we have framed the boundary losses for the primitive variables in the following format:

$$\mathcal{L}_{BC_u} = \frac{1}{N_d}\sum_{i=1}^{N_d}|u(x_i,y_i) - U_i|^2 + \frac{1}{N_n}\sum_{i=1}^{N_n}\left|\frac{\partial u}{\partial n}(x_i,y_i) - U_n\right|^2, \tag{22}$$

$$\mathcal{L}_{BC_v} = \frac{1}{N_d}\sum_{i=1}^{N_d}|v(x_i,y_i) - V_i|^2 + \frac{1}{N_n}\sum_{i=1}^{N_n}\left|\frac{\partial v}{\partial n}(x_i,y_i) - V_n\right|^2, \tag{23}$$

$$\mathcal{L}_{BC_p} = \frac{1}{N_d}\sum_{i=1}^{N_d}|p(x_i,y_i) - P_i|^2 + \frac{1}{N_n}\sum_{i=1}^{N_n}\left|\frac{\partial p}{\partial n}(x_i,y_i) - P_n\right|^2, \tag{24}$$

$$\mathcal{L}_{BC_\theta} = \frac{1}{N_d}\sum_{i=1}^{N_d}|\theta(x_i,y_i) - \theta_i|^2 + \frac{1}{N_n}\sum_{i=1}^{N_n}\left|\frac{\partial \theta}{\partial n}(x_i,y_i) - \theta_n\right|^2. \tag{25}$$

Hence, we can compute the total loss generated in the system due to the boundary values by summing up all the losses shown as follows:

$$\mathcal{L}_{BC} = \mathcal{L}_{BC_u} + \mathcal{L}_{BC_v} + \mathcal{L}_{BC_p} + \mathcal{L}_{BC_\theta}. \tag{26}$$

Once all the losses, depicted in Eqs. (21) and (26), have been evaluated for the boundary value problem, we can now compute the total physics loss corresponding to the given boundary value PDE as

$$\mathcal{L}_p := \mathcal{L}_g + \beta\mathcal{L}_{BC}, \tag{27}$$

where β ($\beta > 0$) is a user-defined weighting coefficient for the boundary condition loss. Notably, we do not have data loss in our problem. Moreover, we have not used any data from simulations or physical experiments for training the PINN.

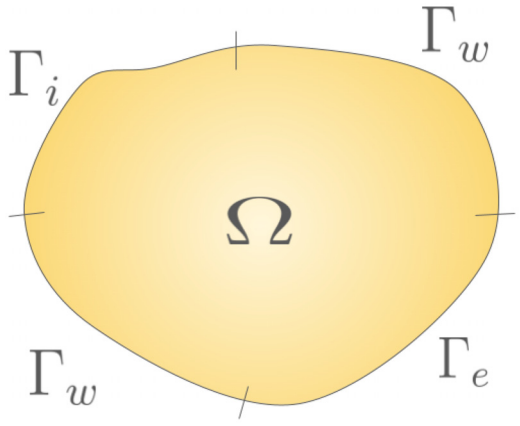

FIG. 5. Generalized computational domain depicting boundary losses comprising of Γ_w for wall losses, Γ_i for inlet boundary losses, and Γ_e for exit boundary losses.

B. Effect of hyperparameters on PINNs performance

The performance of physics-informed neural networks (PINNs) is highly sensitive to the choice of hyperparameters, which requires careful tuning. Key hyperparameters that influence the accuracy of PINNs include the network architecture (such as the number of hidden layers and neurons per layer), the learning rate, the choice of optimizer, the activation function, and the method for initializing the network weights. In this study, we have used Adam optimizer, a first-order stochastic gradient-based method[45] for training the model.

Adam optimizer is highly sensitive to the learning rate chosen. To balance the convergence speed with stability in results, it is important to carefully tune the learning rate. If the learning rate is too low, training can be excessively slow or may become trapped in local minima. Contrarily, a high learning rate could lead to oscillations around local minima, preventing proper convergence. Hence, in this study, we start with a relatively high rate of 10^{-3}. A learning rate scheduler monitors the loss function, adapting the learning rate based on the loss encountered while training. To implement this, we propose a scheduler sub-routine, depicted in Eq. (28), which has not been implemented in any of the previous mentioned literature to the best of the author's knowledge. If the loss does not decrease for 20 consecutive epochs, the learning rate is updated by the following formula:

$$\eta_{t+1} = \max(\eta_{\min}, \eta_t \cdot \gamma), \tag{28}$$

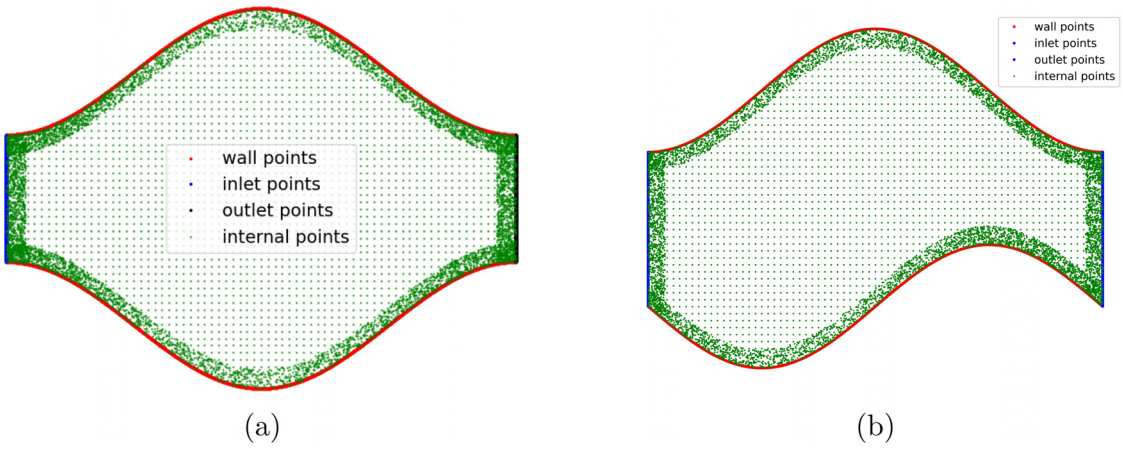

FIG. 6. (a) Symmetric and (b) asymmetric data distributions for the expanded and compressed section of the channel.

where η_t is the current learning rate, η_{min} is the minimum learning rate allowed in the training process, and γ is the learning rate multiplication factor and should be between 0 and 1, so as to simulate a decreasing learning rate behavior. In our case, we have used a learning rate multiplication factor of 0.8 and a minimum learning rate of 10^{-6}. Xavier initialization[46] was applied to initialize the parameters of the neural network, providing a systematic and effective starting point for training.

C. Data generation for DNN model

In PINNs, loss functions are defined across a continuous domain but are evaluated practically at discrete points, known as collocation points. These points are strategically selected using a multidimensional distribution [Latin hypercube sampling (LHS)] on both the domain boundaries and within the interior. Within the domain, the loss corresponding to the governing PDE (referred to as the functional or PDE loss) is calculated, while on the boundaries, a separate loss captures the boundary conditions. This method eliminates the need for traditional grid generation, as shown in Fig. 6(a). For modeling bulk flow along the wavy channel, evenly spaced collocation points are generated across the boundary and throughout the domain's interior. Notably, the collocation points are refined near the walls to better capture the details of the flow.

It is noteworthy of mentioning that PINN is an **unsupervised, meshless deep learning method**, so theoretically does not require any specific arrangement of points but as per the classical CFD notion, it is a good practice to refine the points near the wavy wall boundary, mainly for capturing the boundary layers effects and ensuring accurate wall shear stress and drag calculation. Data generation in a wavy channel presents unique challenges due to its complex geometry. In this study, Latin hypercube sampling (LHS)[47] is utilized to generate collocation data points. To accurately capture flow details, these points are concentrated near the corrugated walls. An elaborate description of the number of points on collocation and boundary points for different cases along with a brief outline of the DNN architecture and hyperparameters are described in Table I.

However, there are ample number of studies that can be cited, which show a random distribution of collocation points inside the computational domain, namely, Villié *et al.*[48] used PINN to assimilate the turbulent mean flow fields from Cartesian time-resolved three-dimensional phase-contrast magnetic resonance imaging [known as four-dimensional (4D) flow MRI] measurements in an *in vitro* axisymmetric stenosis. They have used random sampling of training and collocation points based on Latin hypercube sampling (LHS) to facilitate the forward problem solving since the optimization is based solely on the fulfillment of the PDEs in the artifact region.

IV. VALIDATION OF DNN MODEL

This section focuses on the validation of PINN results and its training process for some benchmark cases so as to establish the confidence on the working and accuracy of the deep learning model. In this study, we have considered two benchmark problems, namely, lid-driven cavity and plane channel flow problem.

A. Loss updates and error residuals during DNN training

In this study, the correctness of the DNN model is verified by performing a mass conservation study on the outputs produced by the DNN model. For this study, an asymmetric wavy channel is considered with a phase shift $\phi = 60°$ in the lower wall, as shown in Fig. 6(b). The loss variations during training for the collocation points and the points at the inlet, outlet, and the wall boundaries are plotted in Fig. 7. The loss is found to decrease gradually with epochs, as

TABLE I. Hyperparameters used in the present study.

Channel type	Architecture[a]	Collocation points	Boundary points	$f(z)$[b]
Plane	5×80	39 600	8000	tanh
Symmetric wavy	6×100	62 000	8000	tanh
Asymmetric wavy	6×100	89 600	9000	tanh

[a]Architecture refers to number of hidden layers × number of nodes per hidden layer used in the PINN model.
[b]$f(z)$: Activation function used, applied layer-wise to introduce non-linearity.

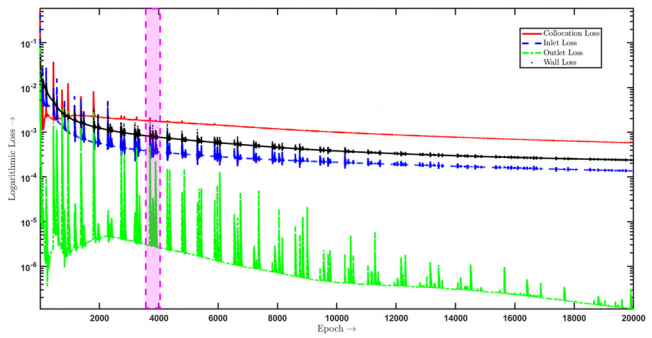

FIG. 7. Prominent loss variations with epochs for the hydrodynamic study decay during the training procedure utilizing the sequential training algorithm. The highlighted zone depicts the point in the training process where the loss function exhibits instability and frequent fluctuations; hence, the loss-based learning rate scheduler intervenes to decrease the learning rate to stabilize loss update.

desired. The spikes in the loss curves represent the points in the training process when the loss update becomes unstable, with rapid fluctuations in the loss obtained. So, the loss-based learning rate scheduler intervenes into the training process and decreases the learning rate to make the loss update stable again. Henceforth, the loss function tends to decrease gradually until the loss update becomes unstable again.

The DNN model is also validated by performing a mass conservation study on the outputs obtained. For this study, the residuals of continuity equation are given in Eq. (10). The residuals are found to be of the order of magnitude 10^{-13}, which can practically be regarded as 0. The residuals obtained for models of varying numbers of layers is plotted in Fig. 8, along with the average squared errors obtained for quantities of interest–cross-stream velocity component u and transverse velocity component v. The average errors for u and v are of the order 10^{-2} and 10^{-3}, respectively, which is well within the errors obtained by Shah and Anand.[40] The continuity residuals and the average squared errors of the quantities of interest are observed to decrease as the number of layers is increased in the DNN model. This shows that the accuracy of the PINN simulation increases as the number of layers in a model is increased.

B. CFD solution

Prior to the comparison of PINN solution with CFD solution, we need to check the dependency of CFD solution on the grid size. The mesh dependency study was conducted using the COMSOL Multiphysics 6.2's custom meshing module, ensuring optimal control of mesh refinement. In Table II, the mean velocity along the centerline for a symmetric sinusoidal channel along with simulation time has been tabulated corresponding to the number of mesh elements.

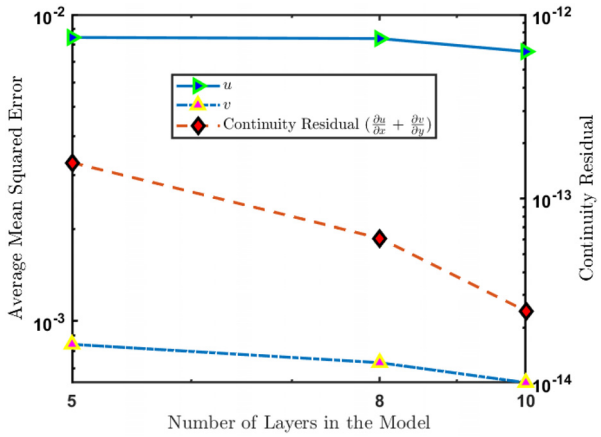

FIG. 8. Continuity residual and average errors of the quantities of interest with respect to CFD simulation for models with varying numbers of layers.

Figure 9 illustrates the effect of **mesh refinement** on the average velocity (u_{avg}) within a sinusoidal symmetrical channel. Initially, as the mesh is refined, u_{avg} decreases due to the improved resolution of boundary layers and flow structures. However, beyond approximately **15,860 elements**, further refinement has minimal impact on u_{avg}, indicating a **mesh-independent solution**. Moreover, a clear trade-off exists between **simulation time** and **mesh elements**. While finer meshes enhance accuracy, they significantly increase computational cost, as evident from the rising blue curve. The selected mesh resolution achieves a balance between **accuracy and efficiency**, making it optimal for capturing the flow physics without excessive computational overhead. To validate the proposed PINN architecture, based on the above-mentioned mesh dependency study, we arrive at the following parameters listed in Table III. We have discretized the pressure and velocity coupling using finite element methodology with second order quadratic Lagrangian elements. Moreover, a successive over-relaxation (SOR) and parallel direct solver are used to solve the linear system iteratively. The parameters used for the simulations are mentioned in the Table III.

1. Lid-driven cavity validation

In the first phase of comparison, we consider a cavity with no-slip walls with the upper lid moving at a uniform velocity, with Reynolds number equal to 100. The axial and transverse velocity components are validated against the pioneering work of Ghia *et al.*[49] and presented in Fig. 10. The present result is observed to be comparable, with difference less than 2%. Hence, the code is assumed to be working well as per the proposed solution. Moreover, the axial and transverse

TABLE II. Mesh elements vs u_{avg} and simulation time.

Mesh elements	Grid 1 216	Grid 2 962	Grid 3 1470	Grid 4 2396	Grid 5 6240	Grid 6 15 910	Grid 7 24 308
u_{avg}	0.28055	0.27430	0.27316	0.27266	0.27183	0.27191	0.27192
Simulation time (s)	1	1	2	2	3	4	5

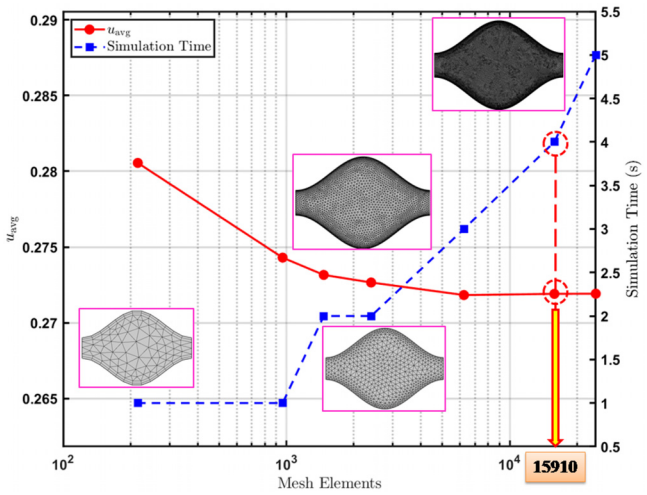

FIG. 9. Mesh independence study.

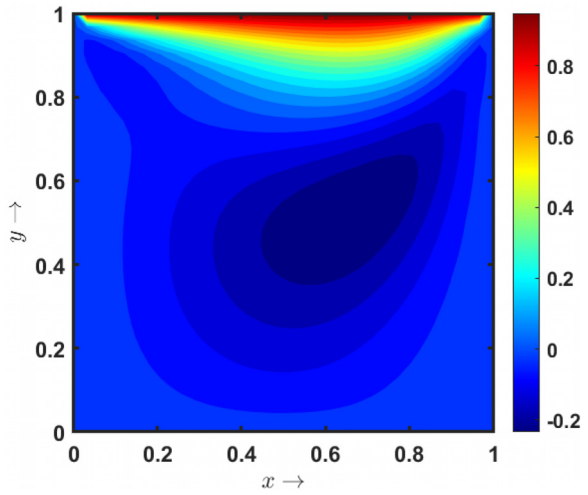

FIG. 10. Contour plot for the streamlines in the lid-driven cavity problem obtained using the proposed PINN architecture, compared with Ghia *et al.*[49]

velocity components are found to be concurrent with the existing literature result as shown in Figs. 11(a) and 11(b).

2. Plane channel flow

To check the accuracy of the model, we have tried to compare the flow field of a plane Poiseuille flow in a parallel plate channel obtained from PINN with CFD simulation. A moderate Re is chosen to capture the behavior of a Newtonian fluid flow through the channel. This configuration ensures that both the developing and fully developed velocity profiles align closely with the reference solution. From Fig. 12(b), the evolution of the velocity profile along the length of the channel is evident. Initially, the flow exhibits a plug-like profile at the inlet, consistent with the imposed boundary conditions. As the flow progresses, viscous boundary layers form and grow, causing the core velocity to evolve. Eventually, the velocity profile reaches a steady, fully developed parabolic shape, providing a laminar flow between parallel plates. From Figs. 12(a) and 12(b), it is concluded that the accuracy and efficiency of the present model is well validated and comparable.

TABLE III. Parameters used in CFD simulation.

Parameter	Value
Total number of elements	15 910
Number of domain elements	15 352
Number of boundary elements	558
Maximum element size	0.0715
Minimum element size	8.25×10^{-4}
Maximum element growth rate	1.08
Curvature factor	0.25
Resolution of narrow regions	1
Fully coupled nonlinear method	Newton (automatic)
Solver	Parallel direct sparse solver interface

V. RESULTS AND DISCUSSION

This section discusses the results obtained from the simulation performed by PINNs, compared with the corresponding CFD data to evaluate the error obtained. Various geometrical and flow parameters are modified to generate flow fields and heat transfer characteristics, which capture the intricate flow dynamics in the wavy geometries.

A. Wavy channel

In this section, the flow field patterns obtained by PINN in the symmetric and asymmetric wavy channels for different Re are presented. Both in-phase and out-of-phase configurations are considered for asymmetric wavy geometries, mimicking the anatomy of tortuous blood vessels.[50] PINN results are compared with conventional CFD results. Absolute errors between PINN and CFD results are also reported as an alternative metric for error analysis compared to relative errors, due to the channel wall curvature. Flow reversal may occur within the wavy sections, leading to recirculation zones. The low velocities within these regions result in near-zero denominators during the relative error calculation, amplifying the error in these areas and making them too unreliable to interpret throughout the domain. Specifically, blood flow hemodynamics are modeled under the Newtonian regime,[51] which can be easily handled by the model for comparison with practical observations.

1. Channel with symmetrical boundaries

This section presents the results of symmetric channel for two distinct cases simulated for different Reynolds numbers (Re = 10 and Re = 80) depicting two varied flow regimes. Figure 13 shows the streamwise velocity (u) contours for the two Re (Re = 10 and Re = 80). The left column [Figs. 13(a) and 13(d)] displays the CFD results, while the middle column [Figs. 13(b) and 13(e)] presents the results from the PINNs. The right column [Figs. 13(c) and 13(f)] highlights the absolute error between the PINNs and CFD predictions.

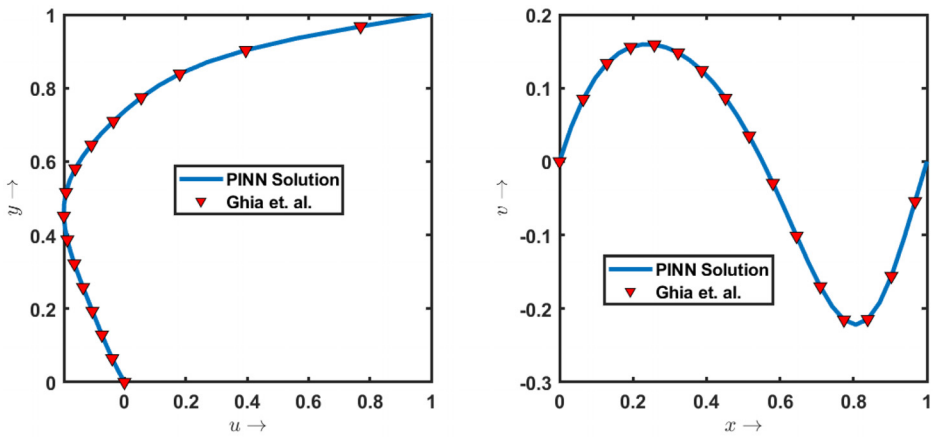

FIG. 11. Comparison of (a) axial (u) and (b) transverse velocities (v) for the lid-driven cavity problem obtained using the proposed PINN architecture, with Ghia *et al.*[49]

PINN contours illustrate that the streamwise velocity reaches its highest magnitude at the inlet and outlet due to the constriction of the cross-sectional area, which accelerates the flow. Because of the symmetry, the velocity distribution remains symmetric about the channel's central axis, as illustrated in Figs. 14(a) and 14(b). The error plots in Figs. 13(c) and 13(f) illustrate that the absolute error is lower at Re = 15. However, as Re increases to 80, the error magnitude grows significantly. Figure 15 shows the cross-stream velocity contours, where the PINNs results exhibit good agreement with the CFD, as indicated by the uniform color bar scaling. Similar to the streamwise velocity, the absolute error in the cross-stream velocity also increases with Re, as depicted in Figs. 15(c) and 15(f).

Based on the mesh dependency study conducted in the previous section, the streamwise velocity profiles have been updated. Figure 14 depicts the plots of the centerline u-velocity variation along the y-axis at specific cross sections (fixed x-locations). A key difference between the velocity profiles at the two Re is the presence of flow reversal, indicated by negative velocities in Fig. 14(b), which is absent in Fig. 14(a). This behavior reflects the formation of recirculation zones at higher Re, captured accurately by the PINNs model. The improved resolution near the wall, achieved by increasing the density of collocation points in the wall-normal direction, ensures that the model captures the flow behavior close to the boundaries effectively. The plots shown are in close agreement with the results obtained by Shah and Anand.[40]

Due to sufficiently enriched grid scheme, a convergent CFD solution is obtained, although it is noteworthy to mention that PINN solution undervalues the corresponding CFD results. This underestimation of the CFD results by the PINN architecture is likely due to grid-based numerical diffusion effects of CFD and the universal approximating nature of neural networks. Unlike CFD, PINN does not suffer from numerical diffusion effects, but might introduce limitations due to the struggle of the gradient descent algorithm to overcome the stiffness in physics-based optimization process. At higher Reynolds numbers, this discrepancy becomes more pronounced due to the increased inertial effects. As a result, PINN fails to capture the sharp gradients in solution, which leads to underestimation of the hydrodynamic flow features, as depicted in Fig. 14(b).

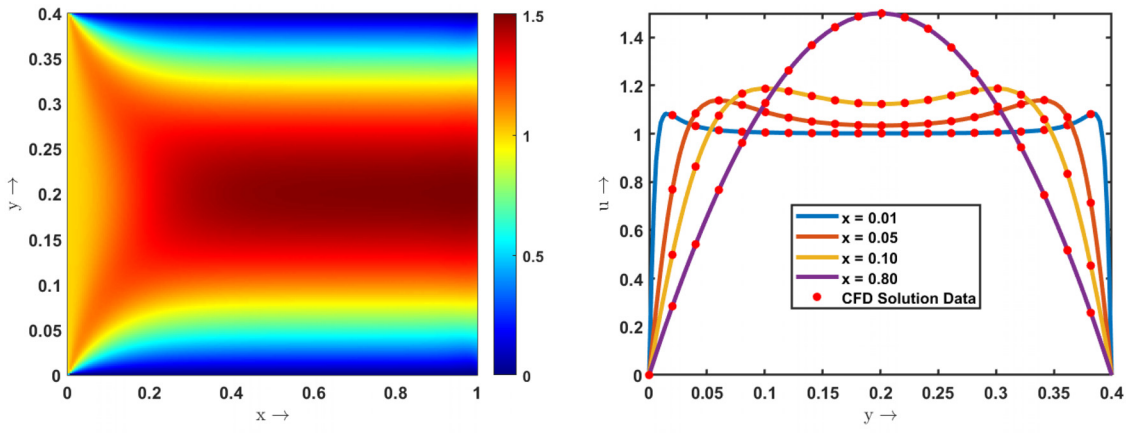

FIG. 12. (a) Velocity contour plot for plane channel flow at Re = 20, where the flow symmetry is preserved at the inlet, and (b) axial velocity profile with respect to y-axis.

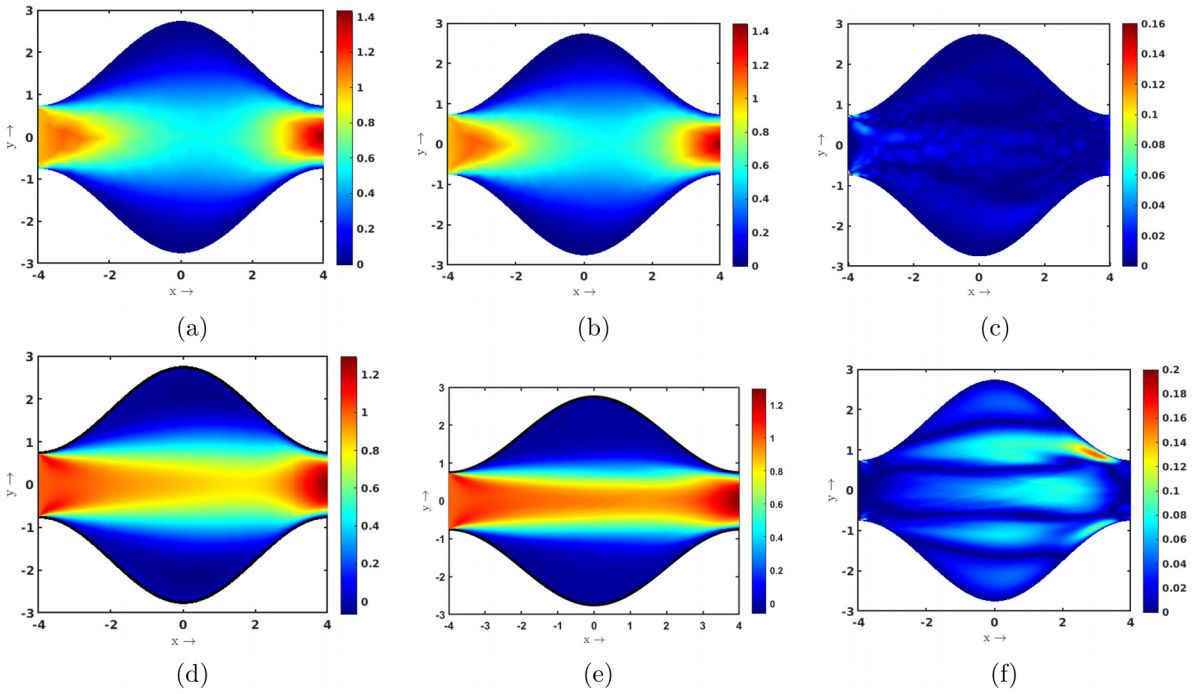

FIG. 13. Streamwise velocity component obtained from (a) CFD simulation and (b) PINN and (c) error for $Re = 10$, $\phi = 0$. Streamwise velocity component obtained from (d) CFD simulation and (e) PINN and (f) error for $Re = 80$, $\phi = 0$.

2. Channel with asymmetric boundaries

In this section, both positive (in-phase) and negative (out-phase) phase shifts between the upper and the lower channel wall are considered. Phase shifts of $\phi = 30°; -30°$, $\phi = 60°; -60°$, $\phi = 90°; -90°$, and $\phi = 180°$ are considered, and their effects on streamwise and cross-stream velocity are highlighted. For our convention, the lower wall moving toward negative x-axis is considered in-phase and the opposite direction is considered out-phase. To simulate the flow in asymmetric wavy channel and mimic the flow regime of blood in blood vessels, a low Reynolds ($Re = 10$) is considered.

Effect of wall heterogeneity on the flow velocity: Figures 16 and 17 depict the streamwise (u) and transverse (v) velocity components for the out-phase asymmetric channels along with the absolute error plots compared to the CFD results. An opposite qualitative flow behavior is seen where higher velocities are observed at the inlet due to constriction in the cross-sectional area compared to in-phase (Figs. 18 and

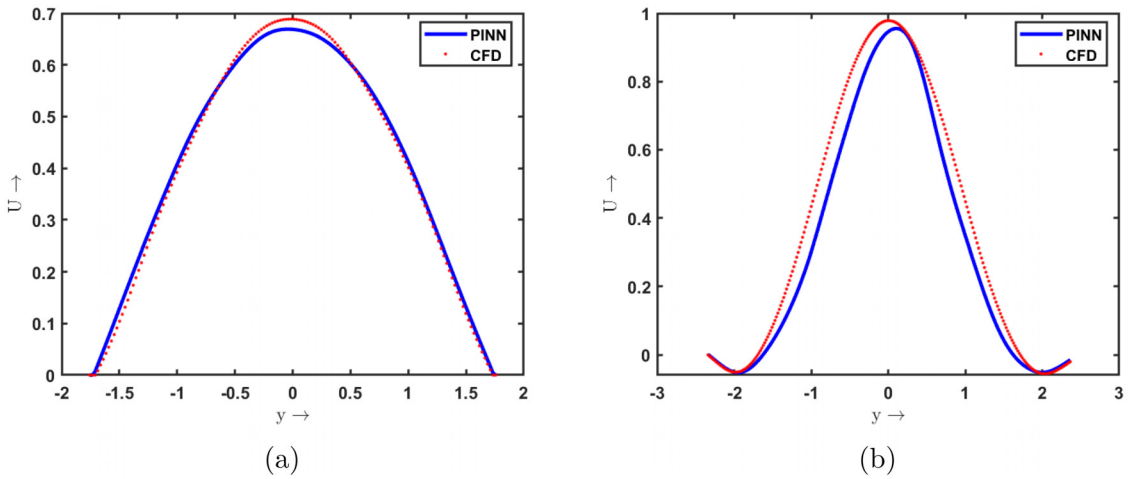

FIG. 14. Streamwise velocity profile at $x = 0$ for (a) $Re = 10$, $\phi = 0$ and (b) $Re = 80$, $\phi = 0$, obtained for both PINN and CFD solutions.

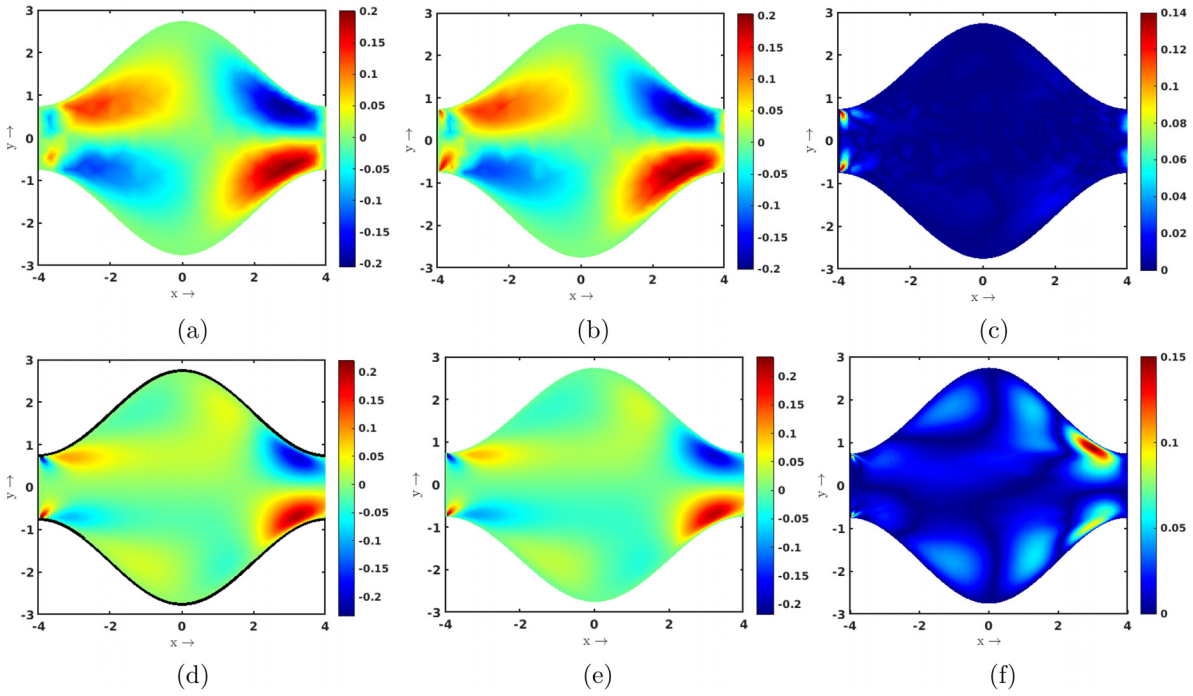

FIG. 15. Cross-stream velocity component obtained from (a) CFD simulation and (b) PINN and (c) error for $Re = 10$, $\phi = 0$. Cross-stream velocity component obtained from (d) CFD simulation and (e) PINN and (f) error for $Re = 80$, $\phi = 0$.

19). Despite dense collocation points near the boundaries, relatively higher errors persist in regions with minimal cross-sectional areas due to the wavy profile of the channel and zero-pressure outlet boundary conditions as the flow does not have enough time to fully develop. The lower wall of the geometry allows the bulk of the fluid to shift toward the exit, facilitating backflow.

The streamwise velocity component (u) for the in-phase asymmetric channels, along with the absolute error plots compared to the CFD results, is shown in Fig. 18. Unlike the symmetric channels where high velocities are confined to the channel inlet and outlet, in asymmetric channels, they are observed at various locations due to variations in the cross-sectional area. For instance, Figs. 18(e) and 18(h) show peak velocity at the channel outlet. Contrarily, Fig. 18(k) shows it near the channel midpoint. Similar to out-phase, relatively higher absolute error is reflected at the channel exits, but to a lesser extent. These minor discrepancies in the PINN results yield a close match with the CFD results. Figure 19 illustrates the transverse (v) velocity component along with the absolute error plots compared with the CFD results. Notably, regions with minimal cross-sectional area exhibit irregular fluctuations in the cross-stream velocity component due to the recirculation zones created by flow reversal. In Fig. 19, the peak streamwise velocity component shifts toward a narrower cross-sectional area, thus disrupting symmetry. The peak velocity shifts between the inner and the outer wall as a function of the crest-trough locations of the wavy channel. Additionally, transverse velocity magnitudes increase with the increase in the phase shift angle ϕ, as illustrated in Fig. 19.

The variation of streamwise velocity component with wall-normal distance for different phase shifts is presented in Figs. 20 and 21 for the out-phase and in-phase asymmetric channels, respectively. In both figures, there is an increase in the magnitude of the maximum streamwise velocity component with an increase in the phase shift due to minimization of the cross-sectional area with the corresponding phase angle ϕ. The velocity profile obtained from PINN in Fig. 20(a) shows discrepancies from the CFD profile due to negative phase shifts toward the outlet. However, despite the mismatch, no-slip boundary condition is preserved along the corrugated walls. Unlike symmetric channels, wherein the flow experiences uniform conditions on both sides of the centerline, velocity profiles exhibit asymmetric behavior around the mean axis, have distorted orientations, and are more slanted to achieve maximum velocity, as the channel walls are not aligned with each other. As a result, the flow near those walls experience more resistance leading to variation in the pressure gradient. This distorts the velocity profile and can cause the flow to be slower near one side of the channel and faster on the other side, leading to an asymmetric velocity distribution.

Figure 20 illustrates the variation of streamwise velocity profile along the wall-normal direction for asymmetric out-phase. Figure 20(a) shows the profile for -30° phase shift with a single peak at the channel center with symmetric decay toward the walls. The peak velocity is moderate, compared to the larger phase shifts. This relatively symmetric shape suggests that a small phase shift does not cause much asymmetry in the velocity distribution as the flow experiences minor effects of the out-of-phase geometry. As the phase shift angle increases and distorts the geometry, the flow asymmetry becomes more pronounced, as shown in Fig. 20(b), due to increased constriction on one side of the channel. Figure 20(c) shows prominent asymmetric pattern with a substantial increase in the magnitude and a pronounced profile skewness, as the velocity gradient near the peak is steeper on one side.

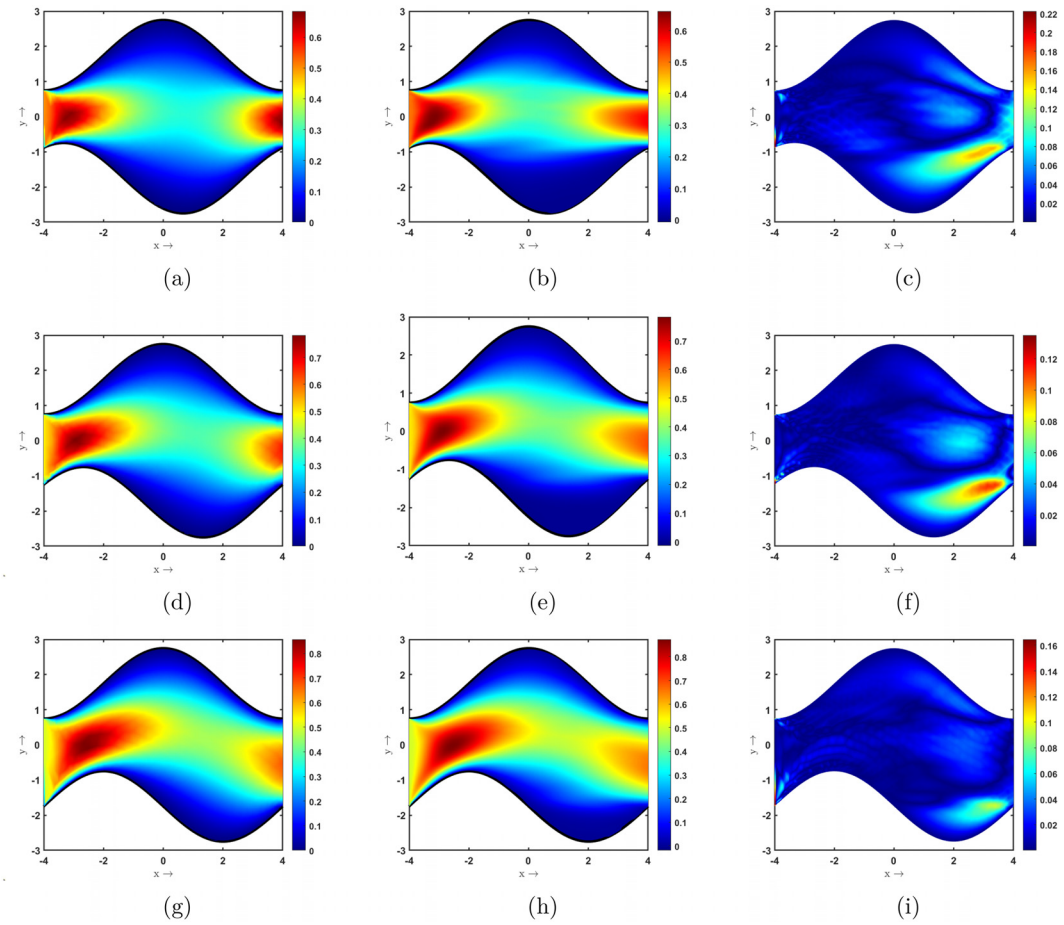

FIG. 16. Streamwise velocity obtained from (a) CFD simulation, (b) PINN, and (c) error for $Re = 10$, $\phi = -30^{\circ}$. Streamwise velocity obtained from (d) CFD simulation, (e) PINN, and (f) error for $Re = 10$, $\phi = -60^{\circ}$. Streamwise velocity obtained from (g) CFD simulation, (h) PINN, and (i) error for $Re = 10$, $\phi = -90^{\circ}$.

The higher peak velocity is due to the greater flow acceleration through these constricted regions, as the fluid experiences greater shear forces and convection effect that produces a larger pressure gradient.

Friction factor: As earlier mentioned by Bahaidarah and Chen,[52] the friction factor for a wavy channel is mathematically defined as

$$f = \frac{[P_m(\mathrm{MI}) - P_m(\mathrm{MO})]H_{\mathrm{av}}}{(L)(2\rho u_{\mathrm{av}}^2)}, \tag{29}$$

where MI and MO stand for module inlet and module outlet, respectively, P_m is the mean pressure, and H_{av} is the average channel height given by

$$H_{av} = \frac{(H_{min} + H_{max})}{2}.$$

Figure 22 illustrates the variation of friction factor (f) with Reynolds number (Re) for a symmetrical sinusoidal wavy channel with periodic inlet and outlet boundary conditions. The friction factor follows a decreasing trend as the Reynolds number increases, characteristic of laminar and transitional flows where viscous effects dominate at a lower Re, while inertial effects become more significant at a higher Re. The data points from the present study show a close agreement with previous pioneering studies by Bahaidarah and Chen[52] and Ničeno and Nobile.[53] Additionally, the best-fit correlation for the friction factor as a function of Reynolds number is computed and given in Eq. (30), which provides an empirical relationship describing the overall trend in the data,

$$logf = -0.75.\log(Re) + 1.13. \tag{30}$$

The close agreement of the present study with the literature confirms the validity of the numerical approach used. The slight deviations observed can be attributed to several factors, including geometrical differences in the wavy channel shape, numerical discretization errors due to differences in mesh resolution and computational schemes, and boundary conditions implementations that may slightly affect the computed friction factor. Additionally, variations in the flow regime, particularly in the transitional range, may introduce minor discrepancies. Despite these factors, the present study successfully captures the expected behavior of the friction factor in a wavy channel and aligns well with previous experimental and numerical findings. This reinforces the understanding that wall undulations significantly influence

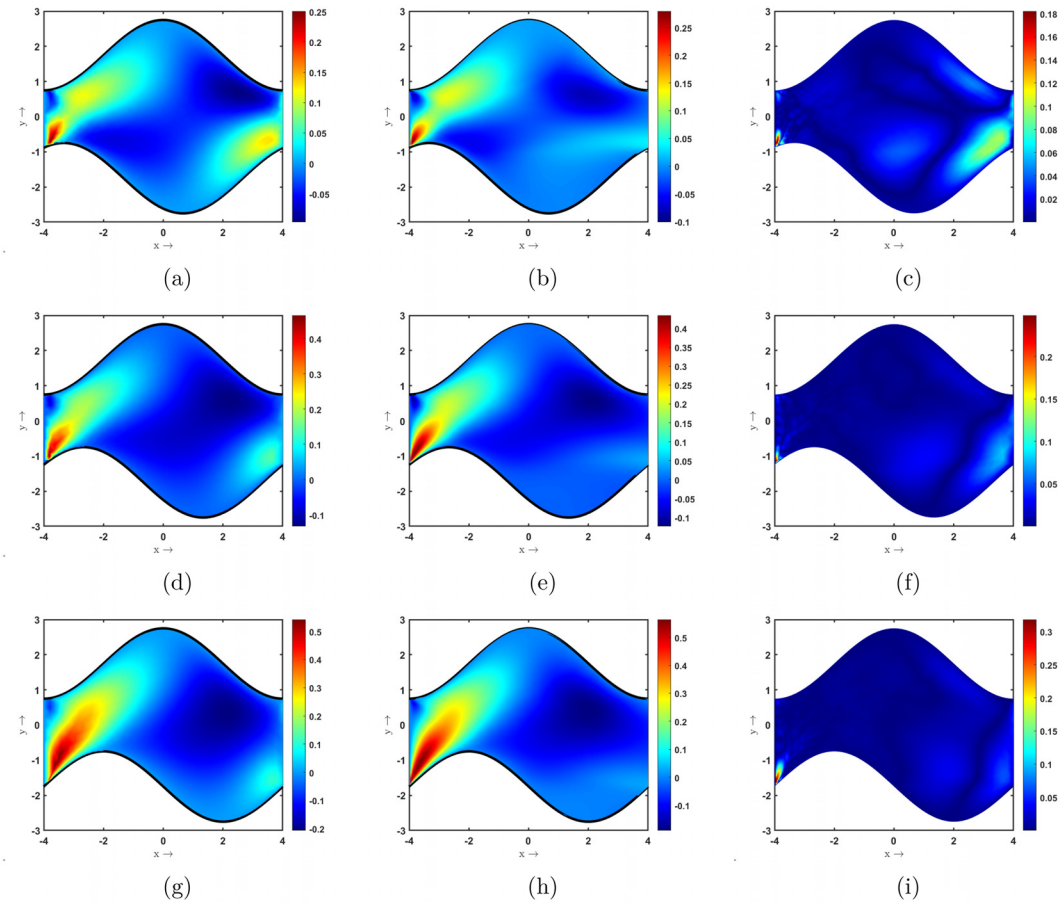

FIG. 17. Cross-stream velocity obtained from (a) CFD simulation, (b) PINN, and (c) error for $Re = 10$, $\phi = -30^{\circ}$. Cross-stream velocity obtained from (d) CFD simulation, (e) PINN, and (f) error for $Re = 10$, $\phi = -60^{\circ}$. Cross-stream velocity obtained from (g) CFD simulation, (h) PINN, and (i) error for $Re = 10$, $\phi = -90^{\circ}$.

flow resistance, particularly at lower Reynolds numbers, where increased surface complexity enhances viscous effects.

Wall Shear Stress variation (WSS): In an asymmetric wavy channel with upper and lower wall phase shifts, the wall shear stress (WSS) distribution is influenced significantly by the local curvature of each wall and the interaction between their phases. Figure 23 depicts the wall shear stress profile variation along the axial direction evaluated on the lower wall. It highlights the flow separation and reattachment points where $\tau = 0$. The wall shear stress magnitude for the lower wall increases significantly as the channel becomes more asymmetric, except in the channel center where there is a relatively less distortion. WSS is found to be higher at the inlet, likely because the boundary layer is initially thin, resulting in a strong velocity gradient near the walls. Since WSS is directly proportional to the velocity gradient at the wall, this boundary layer leads to high WSS near the inlet. As the flow progresses downstream, the boundary layer thickens, reducing the velocity gradient at the wall, consequently reducing WSS. Figure 23(a) depicts the wall shear stress in the stream wise direction in a symmetric channel. The maximum WSS occurs at the narrower parts of the channel (near crests), and the minimum is observed at the wider sections (near troughs). The values are relatively low due to the low Reynolds number, showing a smooth curve without significant oscillations. Contrarily, in a symmetric channel with a relatively higher Reynolds (Re = 80) [Fig. 23(b)], we observe a similar pattern with a higher WSS, indicating stronger velocity gradients near the wall.

Unlike Figs. 23(a) and 23(b), in the remaining plots, the symmetry is lost owing to the asymmetry in the channel geometry. From Fig. 23(c), the peaks of both the in-phase and out-phase can be inferred to not align, resulting in staggered peaks. Thus, the flow experiences varying confinement as it progresses axially. Similarly, in Fig. 23(d), the asymmetry is more pronounced. Figures 23(d) and 23(e) show an irrational increase in the magnitude of WSS at the inlet, because the wavy pattern of the lower wall is shifted in the right direction to that of the upper wall. Thus, the flow profile at the lower wall is closer to a crest, while that at the upper wall is closer to a trough, effectively narrowing the flow path at the inlet. This constriction forces the flow to accelerate more at the inlet, increasing the velocity gradient near the wall and leading to a higher WSS. In the case of 180° phase shift, WSS variations for a lower wall form distinct, mirrored profiles with peaks occurring at opposite axial positions, as shown in Fig. 23(f). Conversely, in the wider sections, the flow has more space to spread out, leading to reduced flow velocity and smaller velocity gradients

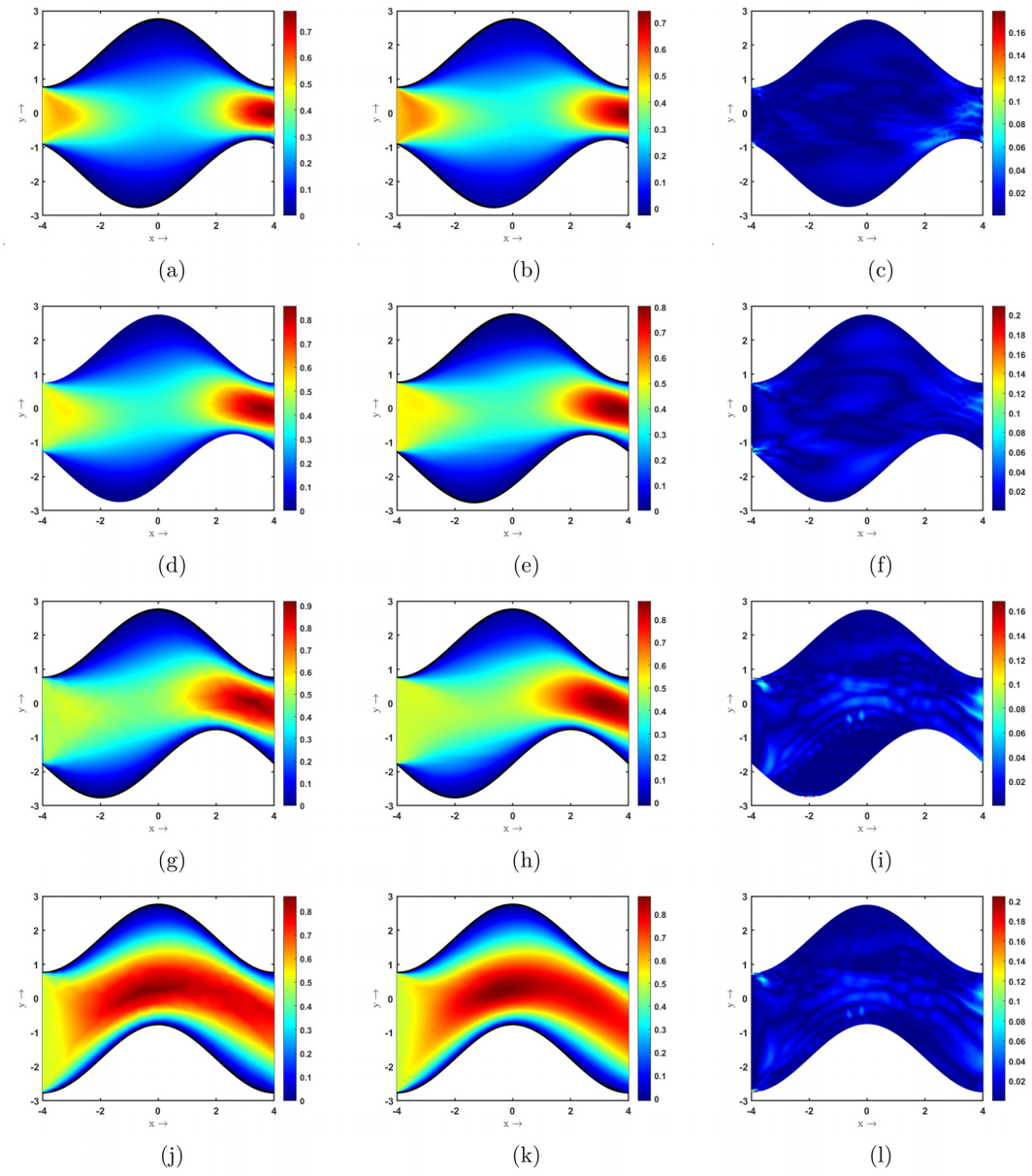

FIG. 18. Streamwise velocity obtained from (a) CFD simulation, (b) PINN, and (c) error for $Re = 10$, $\phi = 30^\circ$. Streamwise velocity obtained from (d) CFD simulation, (e) PINN, and (f) error for $Re = 10$, $\phi = 60^\circ$. Streamwise velocity obtained from (g) CFD simulation, (h) PINN, and (i) error for $Re = 10$, $\phi = 90^\circ$. Streamwise velocity obtained from (j) CFD simulation, (k) PINN, and (l) error for $Re = 10$, $\phi = 180^\circ$.

near the walls, resulting in a lower wall shear stress. As a result, a relatively low WSS is observed than the other profiles for different phase shifts. The peaks in wall shear stress arise due to flow acceleration in the constricted regions. As the fluid is forced to speed up to pass through these narrow sections, the increased velocity near the wall results in a higher shear stress. The peaks represent the points where the velocity gradient is the steepest due to both wall proximity and high flow velocity, together creating a strong shear forces at the wall.

Pressure drop across the channel: This section illustrates a comprehensive outline of the stream wise variation of pressure drop within the corrugated channel. It is important to study this feature as it contributes to the asymmetric flow rate distribution inside the channel. Moreover, the pressure drop can be attributed to the hydraulic resistance offered across the asymmetric channel module. The pressure drop is evaluated with respect to the exit gauge pressure $p = 0$. Figures 24 and 25 vividly illustrate the pressure drop variation in both symmetric and asymmetric (both in-phase and out-of-phase channels).

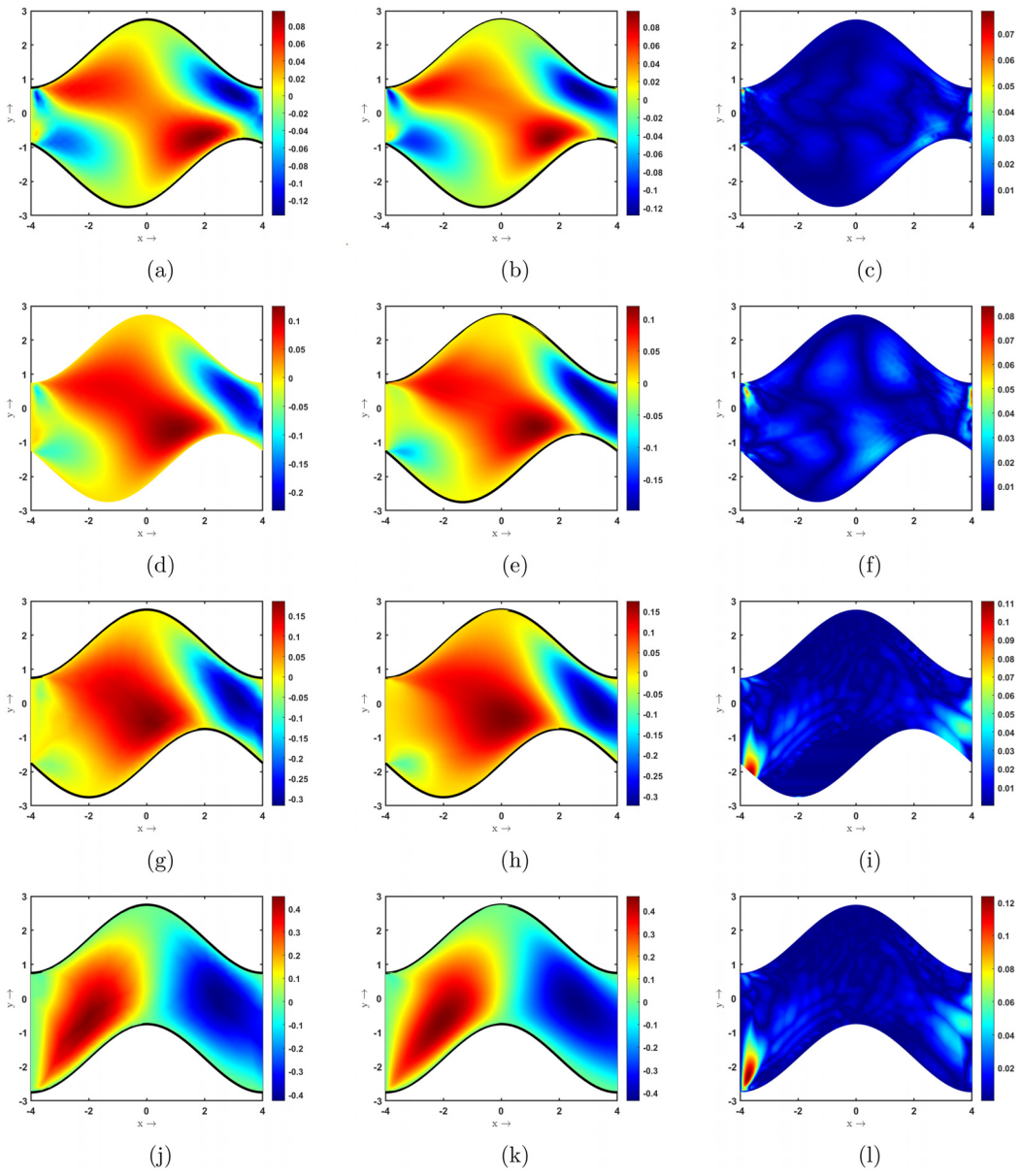

FIG. 19. Cross-stream velocity obtained from (a) CFD simulation, (b) PINN, and (c) error for $Re = 10$, $\phi = 30^\circ$. Cross-stream velocity obtained from (d) CFD simulation, (e) PINN, and (f) error for $Re = 10$, $\phi = 60^\circ$. Cross-stream velocity obtained from (g) CFD simulation, (h) PINN, and (i) error for $Re = 10$, $\phi = 90^\circ$. Cross-stream velocity obtained from (j) CFD simulation, (k) PINN, and (l) error for $Re = 10$, $\phi = 180^\circ$.

Notably, several factors are responsible for pressure drop variation, like phase shift angle, friction factor, and re-absorption coefficient. To maintain brevity of the study, we have restricted ourselves to studying the effect of pressure drop with phase shift angle.

From Fig. 24, it can be noted that as the width of the channel contracts, the pressure drop increases significantly. On the contrary, at the other end of the channel, the pressure drop is equal to zero, as it satisfies the exit pressure boundary condition. Additionally, we observe that the relative magnitude of pressure drop is lower in the case of higher Reynolds numbers in comparison with lower Reynolds numbers. This observation can be justified using the non-dimensional pressure drop (Δp), given by the following equation:

$$\Delta p = \frac{\Delta p^*}{\rho u_{\text{avg}}^{*2}}. \tag{31}$$

It is evident from the above-mentioned equation that with an increase in the Reynolds number, the average velocity increases. Conversely, using Eq. (31), the average velocity is decreased.

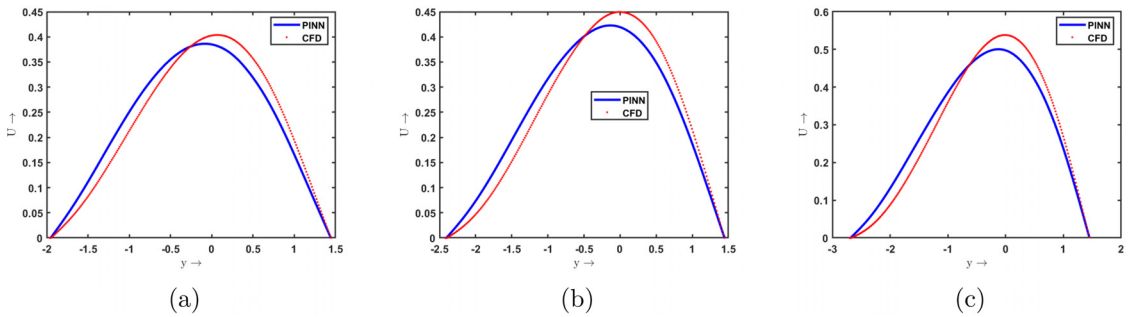

FIG. 20. Streamwise velocity profile for (a) $Re = 10$, $\phi = -30^\circ$, (b) $Re = 10$, $\phi = -60^\circ$, and (c) $Re = 10$, $\phi = -90^\circ$ obtained for both PINN and CFD solutions.

Particularly, from Fig. 25, it is observed that at the channel entrance, the pressure drop for the symmetric case is more than the asymmetric case. This happens because the contraction area no longer lies at the entrance with the phase shift. However, among the asymmetric cases, the highest pressure drop at the entrance is observed for 90° phase shift, irrespective of in-phase or out-phase cases. Moreover, a local minimum is observed for out-of-phase asymmetric channels due to the increase in the average velocity (u_{avg}) at the center of the channel, resulting in a rapid decrease in the magnitude of the pressure drop. The reverse phenomenon is observed for in-phase asymmetric channels. An interesting feature of Fig. 25 is the pressure drop variation at a phase shift of 180°. The patterns of pressure drop for an in-phase shift of 180°, depicted in Fig. 25(b), do not resemble the pattern as depicted by the other in-phase pressure drop plots.

B. Thermal characteristics of wavy channel

In this section, the PINN architecture is implemented in the wavy geometry, which can be extended further for any complex geometries.

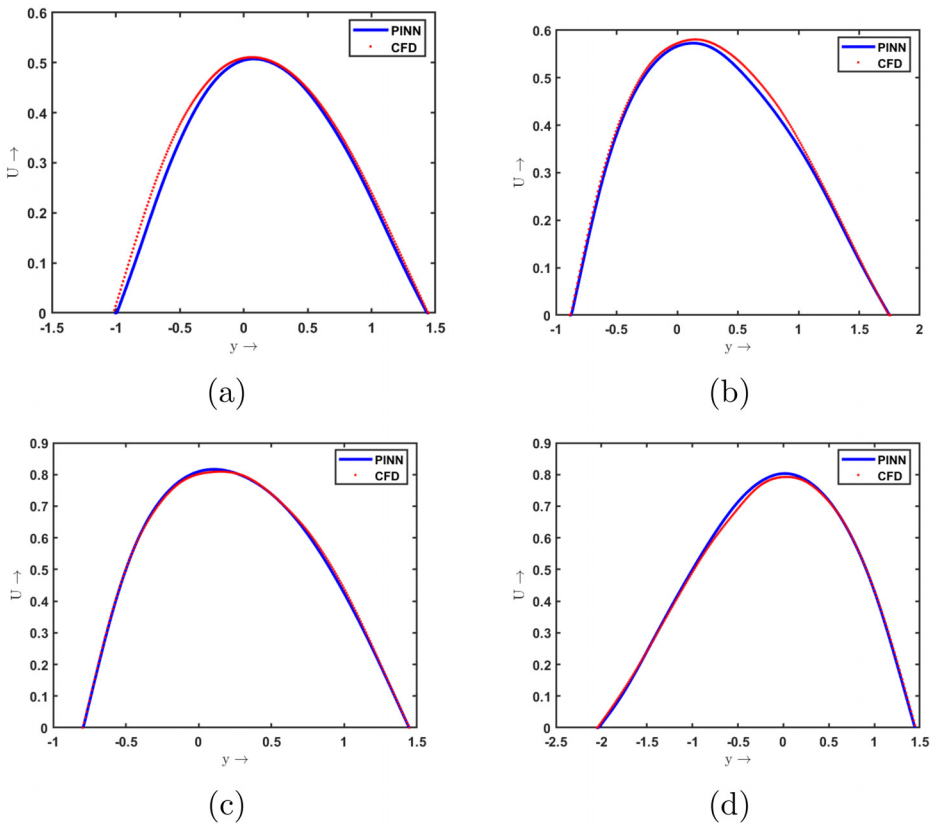

FIG. 21. Streamwise velocity profile for (a) $Re = 10$, $\phi = 30^\circ$, (b) $Re = 10$, $\phi = 60^\circ$, (c) $Re = 10$, $\phi = 90^\circ$, and (d) $Re = 10$, $\phi = 180^\circ$ obtained for both PINN and CFD solutions.

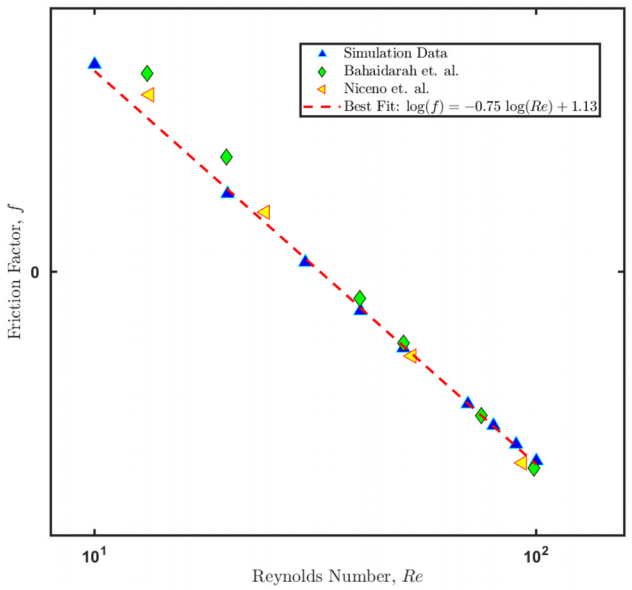

FIG. 22. Variation of friction factor with Reynolds number in the third module of sinusoidal wavy channel depicted in Fig. 1, validated against Bahaidarah and Chen[52] and Ničeno and Nobile.[53]

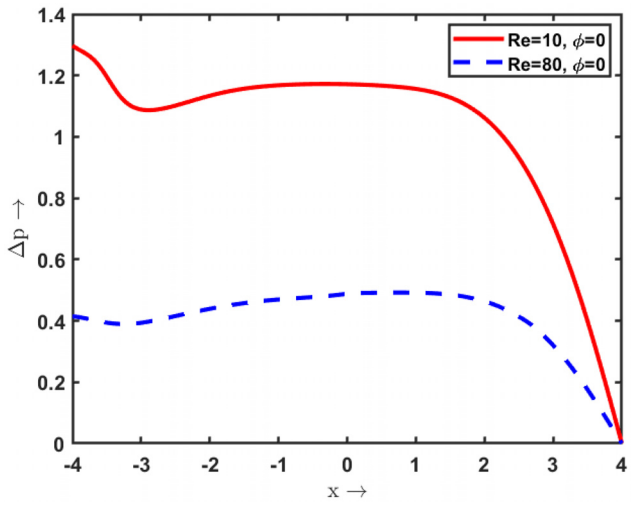

FIG. 24. Pressure drop along the axial direction in a symmetric channel with variation of Reynolds numbers and zero phase shift.

To explore the heat transfer effect for the thermal analysis of flow inside wavy channel, we have restricted ourselves to symmetric channels only with both uniform and non-uniform temperature distribution along the wavy walls.

1. Homogenous temperature distribution on wavy walls

Figures 26–29 represent the temperature distribution for different Reynolds numbers keeping the Prandtl number (Pr) constant to 0.7. At low $Re = 5$, we have observed that the temperature within the fluid reduces significantly. Along the walls of the passage, a thermal boundary layer forms, representing a circulation region where temperature

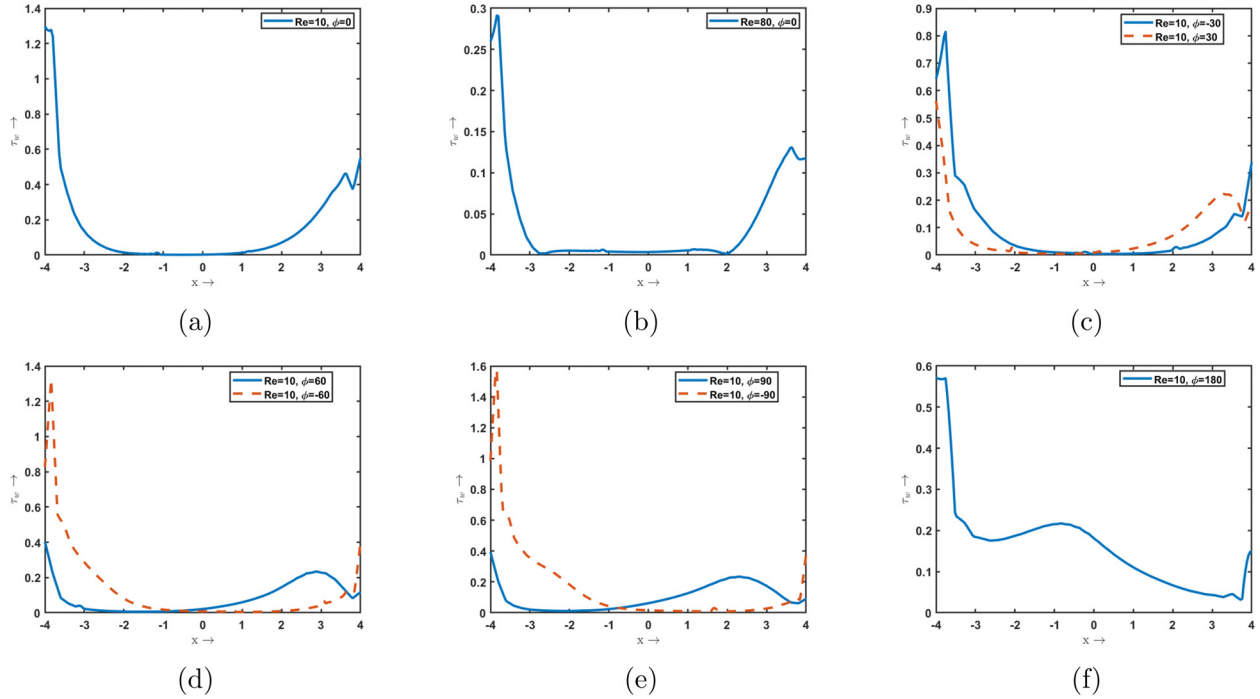

FIG. 23. WSS variation along stream for (a)$Re = 10, \phi = 0^\circ$, (b) $Re = 80, \phi = 0^\circ$, (c) $Re = 10, \phi = 30^\circ, -30^\circ$, (d) $Re = 10, \phi = 60^\circ, -60^\circ$, (e) $Re = 10, \phi = 90^\circ, -90^\circ$, and (f) $Re = 10, \phi = 180^\circ$.

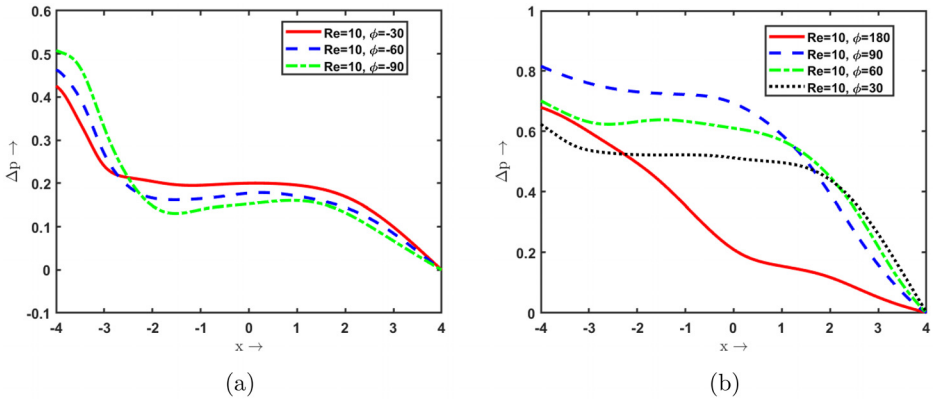

FIG. 25. Variation of pressure drop along the axial direction in asymmetric channel with (a) out-phase shifts ($Re = 10$, $\phi = -30^\circ$, $Re = 10$, $\phi = -60^\circ$, and $Re = 10$, $\phi = -90^\circ$) and (b) in-phase shifts ($Re = 10$, $\phi = 30^\circ$, $Re = 10$, $\phi = 60^\circ$, $Re = 10$, $\phi = 90^\circ$, and $Re = 10$, $\phi = 180^\circ$).

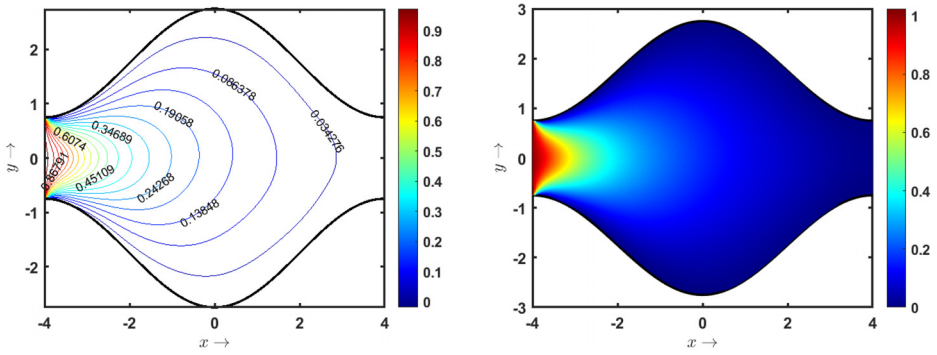

FIG. 26. (a) Isotherm and (b) surface plot for homogenous temperature distribution at $Re = 5$, $Pr = 0.7$ in the expanded part of the cross section.

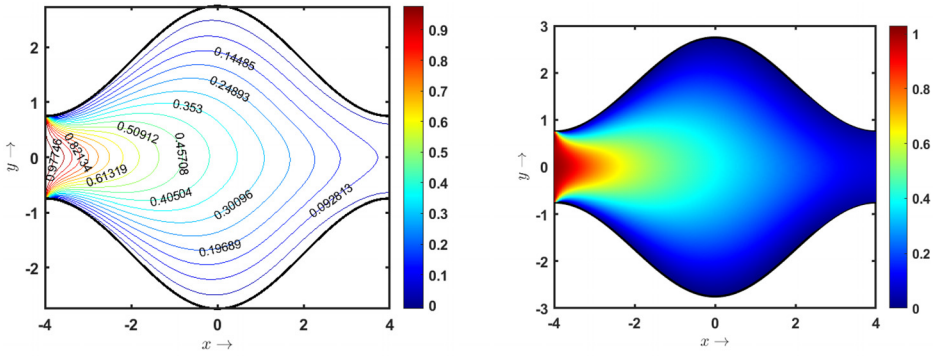

FIG. 27. (a) Isotherm and (b) surface plot for the homogenous temperature distribution at $Re = 10$, $Pr = 0.7$ in the expanded part of the cross section.

gradients are the most pronounced. Within this layer, heat transfer between the walls and the fluid layers is dominated, leading to a gradual establishment of a thermal equilibrium. The thickness of the boundary layer typically increases downstream as the fluid absorbs or loses heat, depending on the thermal conditions of the walls. The temperature contour for $Re = 5$ and 10, as shown in Figs. 26 and 27, is in accordance with that of pioneering study of Wang and Vanka.[12]

As the Reynolds number increases, the temperature profiles within the recirculation regime begin to exhibit significant distortion, as shown in Figs. 28 and 29 for $Re = 20$ and 50, respectively. This distortion is caused by the enhanced mixing and chaotic flow patterns introduced by the growing eddies. As a result, the previously established thermal boundary layer is disrupted and effectively destroyed by the turbulent motion. Notably, near the reattachment point, where the flow transitions back to a more streamlined pattern after separation, the temperature gradient is steeper than that observed near the separation point. This increased gradient near the reattachment zone is due to an intensified heat transfer driven by the stronger interaction

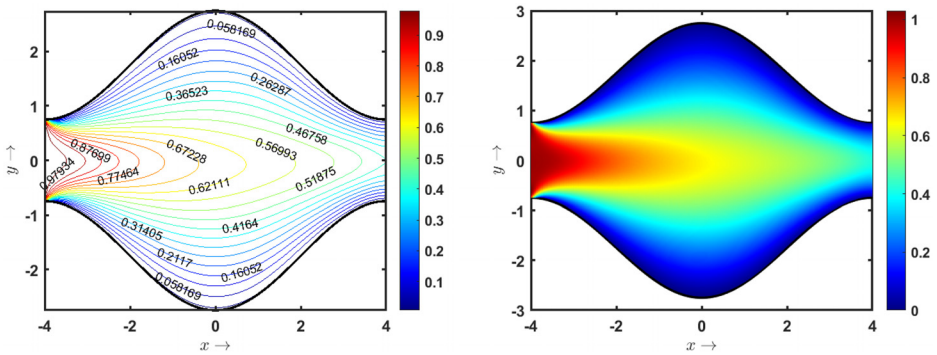

(a) (b)

FIG. 28. (a) Isotherm and (b) surface plot for homogenous temperature distribution at $Re = 20$, $Pr = 0.7$ in the expanded part of the cross section.

between the fluid and the surface, highlighting the complex interplay between flow dynamics and thermal behavior in high Reynolds number regimes.

We can define the local Nusselt number as

$$Nu = \frac{hD_h}{K} = \frac{D_h}{\theta_m}\frac{\partial\theta}{\partial n}. \tag{32}$$

Here, h is the convection heat transfer coefficient, the hydraulic diameter (D_h) is defined as twice the average height (H_m), and θ_m is the bulk mean temperature,

$$\frac{\partial\theta}{\partial n} = \frac{-\frac{\partial f}{\partial x}\frac{\partial\theta}{\partial x} + \frac{\partial\theta}{\partial y}}{\sqrt{1 + \left\{\frac{\partial f}{\partial x}\right\}^2}}$$

and

$$f(x) = y_{\text{top}} = \sin\left(Bx + \frac{\pi}{2}\right) + \left(\frac{H_{\min}}{2} + a\right).$$

Therefore,

$$\frac{\partial\theta}{\partial n} = \frac{-B\cos\left(Bx + \frac{\pi}{2}\right)\frac{\partial\theta}{\partial x} + \frac{\partial\theta}{\partial y}}{\sqrt{1 + B^2\cos^2\left(Bx + \frac{\pi}{2}\right)}}. \tag{33}$$

From Fig. 30(b), it can be inferred that the optimum heat transfer in terms of Nusselt numbers is observed near the expanded and contracted cross sections of the wavy channel, respectively. This behavior can be attributed to the minimum cross section, and the flow velocity increases with constriction, enhancing convective heat transfer and leading to higher Nusselt numbers. Conversely, at the maximum cross section, the flow velocity decreases, reducing convective effects and resulting in low Nusselt numbers.

Furthermore, the local Nusselt number increases with the Reynolds number, as depicted in Fig. 30(a). This occurs because, at higher Reynolds numbers, the temperature gradients near the minimum cross section become steeper due to intensified convective heat transfer. The combination of recirculation eddies and flow acceleration in the constricted regions further amplifies this effect, leading to a more pronounced variation in the Nusselt number distribution.

2. Non-homogeneous temperature distribution along wavy walls

To observe the variation in the heat transfer rate in complex network systems, a sinusoidal heat transfer condition is considered along the wavy walls. Thermal and flow behavior is highly influenced by sinusoidal geometry of the wavy channel, as shown in Fig. 31(a). The thermal and flow behavior, subjected to non-homogeneous temperature boundary conditions, was analyzed for varying Reynolds (Re) and Prandtl (Pr) numbers. As shown in Fig. 31(b), the upper and lower

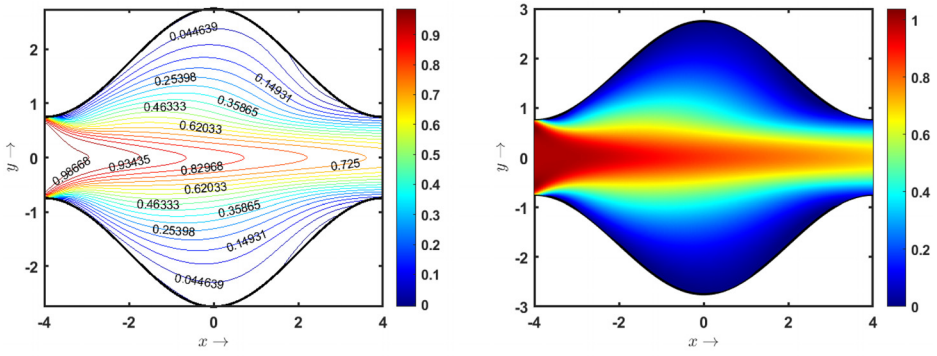

(a) (b)

FIG. 29. (a) Isotherm and (b) surface plot for homogenous temperature distribution at $Re = 50$, $Pr = 0.7$ in the expanded part of the cross section.

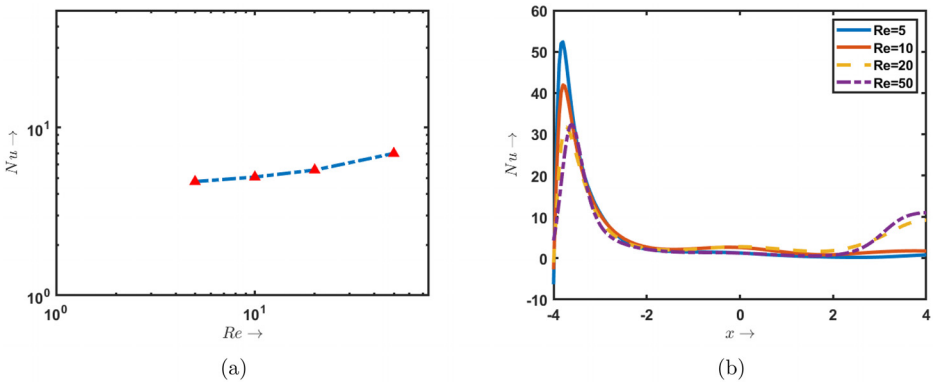

FIG. 30. Variation of Nusselt number (a) with low and moderate Reynolds number, taken on logarithmic scale, and (b) along the axial direction for different Reynolds numbers ($Re = 5, 10, 20, 50$).

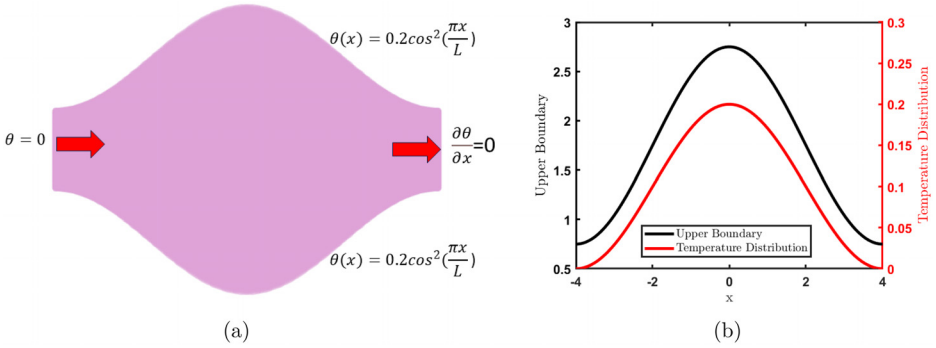

FIG. 31. (a) Temperature boundary conditions applied on the domain and (b) variation of the temperature boundary condition along the side-walls.

walls of the channel were assigned a spatially varying temperature profile, given by the following equation:

$$\theta(x) = 0.2\cos^2(\pi x/L). \tag{34}$$

At inlet, the boundary condition for the temperature is set to 0, while the streamwise velocity component is set to 1 in non-dimensional form. The outlet has a zero temperature gradient and zero-pressure boundary condition. The simulation results, presented through contour and surface plots, provide insight into the heat transfer characteristics and flow dynamics under different thermal-fluid conditions.

Figure 32 depicts the temperature profiles for $Re = 20$ and $Pr = 0.5$. The contour plot [Fig. 32(c)] shows broader and smoother temperature gradients compared to Fig. 33(c). The surface plot reveals a more uniform temperature distribution. The lower Prandtl number, indicating a higher thermal diffusivity, promotes more effective heat diffusion throughout the fluid, resulting in reduced temperature gradients despite the minimal convective effects. Figure 33 illustrates the contour and surface plots for temperature distribution for $Re = 20$ and $Pr = 0.7$, respectively. The contour plot [Fig. 33(c)] reveals smooth and symmetric temperature gradients, indicating a diffusion-dominated heat transfer regime. The surface plot shows a gradual

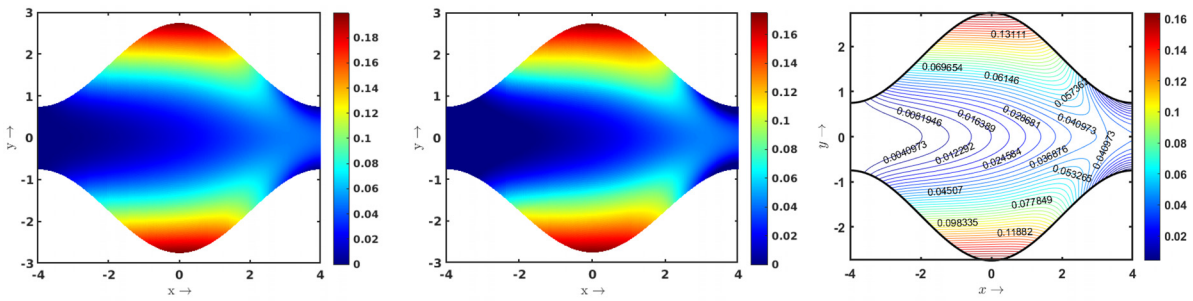

FIG. 32. Surface plots for (a) PINN and (b) CFD simulations. (c) Isotherm for PINN simulation of non-homogenous temperature distribution for $Re = 20$; $Pr = 0.5$ in the expanded part of the cross section.

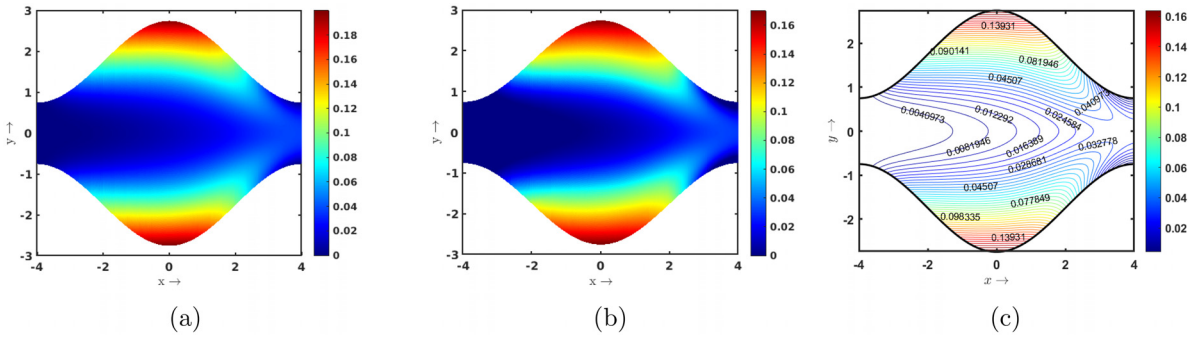

FIG. 33. Surface plots for (a) PINN and (b) CFD simulations. (c) Isotherm for PINN simulation of non-homogenous temperature distribution for $Re = 20$; $Pr = 0.7$ in the expanded part of the cross section.

decrease in temperature from the heated walls to the cooler core of the flow. As the Reynolds number is low, viscous forces dominate, resulting in weak convective heat transfer. Moderate Prandtl number suggests comparable thermal and momentum diffusivities, leading to predominantly conductive heat transfer. In Fig. 34, the results for $Re = 50$ and $Pr = 0.7$ are shown. The contour plot [Fig. 34(c)] displays elongated and compressed temperature contours near the walls, reflecting stronger convection effects. The surface plot highlights greater asymmetry in the temperature field, with cooler regions extending deeper into the flow. A higher Reynolds number amplifies inertial forces, enhancing convective heat transport and disrupting the symmetry seen at lower Reynolds numbers.

The comparison between computational fluid dynamics (CFD) simulations and physics-informed neural networks (PINN) simulations highlights key differences in the predicted temperature fields. The results indicate that PINN consistently underestimates the temperature variation, producing a lower upper bound compared to CFD. This disparity arises due to the nature of PINN's approximation capabilities, which depend on the training data, physics constraints, and loss function optimization. While CFD solves the governing equations using discretization and numerical schemes, PINN approximates the solution based on a learned function, which can smooth out variations, especially in complex boundary conditions and high-gradient regions. The underestimation by PINN suggests that it struggles to capture the sharp thermal gradients near the wavy walls, likely due to limitations in its ability to resolve localized temperature variations. However, despite this deviation, PINN maintains the overall temperature distribution trends, indicating its potential for data-efficient surrogate modeling while acknowledging the need for further refinement in training strategies to enhance accuracy near boundary layers.

In summary, increasing the Reynolds number enhances the convective heat transfer, evident from sharper temperature gradients and deeper cooling penetration. Lowering the Prandtl number improves thermal diffusion, leading to a more uniform temperature field. The sinusoidal geometry further affects heat transfer by inducing flow separation and recirculation zones, especially at higher Reynolds numbers. Optimizing flow and thermal parameters is crucial to achieving effective thermal performance in complex geometries.

VI. CONCLUSION

In this article, a fully unsupervised novel PINN architecture is developed to capture the intricate flow dynamics and heat transfer characteristics in a wavy channel. Asymmetricity inside the wavy channels is considered by taking the in-phase and out-phase shifts of various magnitudes. PINN results are validated with CFD results obtained from COMSOL Multiphysics simulations, and absolute errors are reported. For the forward PINN problem, while reproducing the flow field in asymmetric channels (with in-phase and out-phase angular shifts in the lower wall boundary), a peak absolute error of 22% and 18% for the axial and transverse components of velocity, respectively,

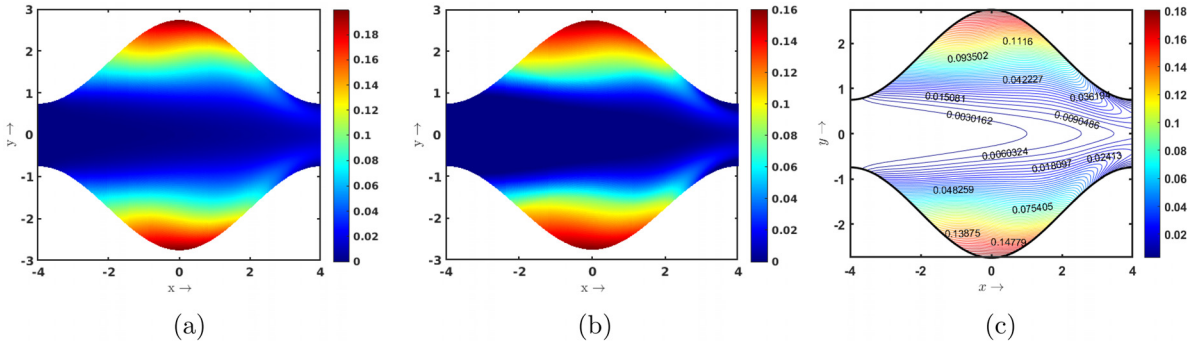

FIG. 34. Surface plots for (a) PINN and (b) CFD simulations. (c) Isotherm for PINN simulation of non-homogenous temperature distribution for $Re = 50$; $Pr = 0.7$ in the expanded part of the cross section.

is encountered over the spatial domain. The errors in the results obtained in this study are significantly lower than Shah and Anand,[40] owing to the novel PINN architecture and the learning rate scheduler. In addition, the study demonstrates that PINN can capture intricate flow features, such as flow reversal and recirculation regions in asymmetric wavy channels. To accelerate convergence during training, a robust scheduler subroutine has been developed that dynamically adjusts learning rate based on the loss obtained in an epoch. This approach allows the training process to begin with a significantly higher learning rate compared to earlier works (Shah and Anand[40]) while effectively reducing the loss to lower values with the less epochs in training. Moreover, we tried to analyze the heat transfer characteristics in this wavy channel by implementing both uniform and a sinusoidal temperature along the walls of the wavy geometry, using an additional neural network output for scalar temperature field. It enabled us to explore the effects of local Nusselt number variation and its correlation with the characteristics Reynolds number of the flow. This ultimately leads us to infer the enhancement in heat transfer in wavy channels in comparison with plane channels. These results for heat transfer characteristics are instrumental in designing an efficient heat exchange device, which has immense applications in biological tissue heat transfer as well as in industrial horizons. For the future scope of this work, we will try to eliminate the limitations of the present deep learning architecture so that the flow physics can be analyzed at a higher Reynolds number in a transient fashion. This will enable us to capture the laminar to turbulent transition effects.

ACKNOWLEDGMENTS

The authors are thankful to the Science and Engineering Research Board (SERB), India, for providing financial support for the preparation of the paper.

AUTHOR DECLARATIONS

Conflict of Interest

The authors have no conflicts to disclose.

Author Contributions

Aritra Roy: Conceptualization (equal); Formal analysis (equal); Investigation (equal); Validation (equal); Visualization (equal); Writing – original draft (equal). **Ayan Mukherjee:** Investigation (equal); Methodology (equal); Resources (equal); Software (equal); Validation (equal); Writing – original draft (equal). **Balbir Prasad:** Data curation (equal); Methodology (equal); Resources (equal); Software (equal); Visualization (equal). **Ameeya Kumar Nayak:** Conceptualization (equal); Methodology (equal); Supervision (equal); Writing – review & editing (equal).

DATA AVAILABILITY

The data that support the findings of this study are available from the corresponding author upon reasonable request.

REFERENCES

[1]M. Gibreel, X. Zhang, and H. Elmouazen, "Serpentine and furrowed wavy channels-based enhancement in heat transfer for a rocket engine chamber," Int. J. Therm. Sci. **185**, 108074 (2023).
[2]D. Ram, D. S. Bhandari, D. Tripathi, and K. Sharma, "Motion of bacteria and CaOx particles via urine flow modulated by the electro-osmosis," Phys. Fluids **35**(12), 121910–121912 (2023).
[3]M. Nagargoje and R. Gupta, "Effect of asymmetry on the flow behavior in an idealized arterial bifurcation," Comput. Methods Biomech. Biomed. Eng. **23**, 232–247 (2020).
[4]S. Xinhui, L. Zhemg, X. Zhang, S. Xinyi, and L. Min, "Asymmetric viscoelastic flow through a porous channel with expanding or contracting walls: A model for transport of biological fluids through vessels," Comput. Methods Biomech. Biomed. Eng. **17**, 623 (2014).
[5]J. C. Burns and T. Parkes, "Peristaltic motion," J. Fluid Mech. **29**(4), 731–743 (1967).
[6]I. J. Sobey, "On flow through furrowed channels. Part 1. Calculated flow patterns," J. Fluid Mech. **96**(1), 1–26 (1980).
[7]K. Stewartson and P. G. Williams, "On self-induced separation II," Mathematika **20**(1), 98–108 (1973).
[8]K. D. Stephanoff, I. J. Sobey, and B. J. Bellhouse, "On flow through furrowed channels. Part 2. Observed flow patterns," J. Fluid Mech. **96**(1), 27–32 (1980).
[9]P. Hall, "Unsteady viscous flow in a pipe of slowly varying cross-section," J. Fluid Mech. **64**(2), 209–226 (1974).
[10]D. F. Young and F. Y. Tsai, "Flow characteristics in models of arterial stenoses—I. Steady flow," J. Biomech. **6**(4), 395–410 (1973).
[11]T. Nishimura, Y. Ohori, and Y. Kawamura, "Flow characteristics in a channel with symmetric wavy wall for steady flow," J. Chem. Eng. Jpn. **17**(5), 466–471 (1984).
[12]G. Wang and S. Vanka, "Convective heat transfer in periodic wavy passages," Int. J. Heat Mass Transfer **38**(17), 3219–3230 (1995).
[13]C. Liu, Y. Bao, B. Li, P. Lyu, X. Liu, and Z. Rao, "Experimental study on heat transfer enhancement and flow performance of microencapsulated phase change slurry in microchannel with different rib structures," Int. J. Heat Mass Transfer **237**, 126437 (2025).
[14]J. Benhamou, S. Channouf, M. Jami, and A. Mezrhab, "Application of acoustic waves to heat transfer enhancement," AIP Conf. Proc. **2580**, 020006 (2023).
[15]G. J. Brereton and S. M. Jalil, "Diffusive heat and mass transfer in oscillatory pipe flow," Phys. Fluids **29**(7), 073601 (2017).
[16]J. E. O'Brien and E. M. Sparrow, "Corrugated-duct heat transfer, pressure drop, and flow visualization," J. Heat Transfer **104**(3), 410–416 (1982).
[17]M. M. Ali and S. Ramadhyani, "Experiments on convective heat transfer in corrugated channels," Exp. Heat Transfer **5**(3), 175–193 (1992).
[18]L. Zhang, R. Duan, Y. Che, Z. Lu, X. Cui, L. Wei, and L. Jin, "A numerical analysis of fluid flow and heat transfer in wavy and curved wavy channels," Int. J. Therm. Sci. **171**, 107248 (2022).
[19]W. Zhou, S. Miwa, and K. Okamoto, "Advancing fluid dynamics simulations: A comprehensive approach to optimizing physics-informed neural networks," Phys. Fluids **36**(1), 013615 (2024).
[20]P. Pant, R. Doshi, P. Bahl, and A. Barati Farimani, "Deep learning for reduced order modelling and efficient temporal evolution of fluid simulations," Phys. Fluids **33**(10), 107101–107110 (2021).
[21]K. Fukushima, "Visual feature extraction by a multilayered network of analog threshold elements," IEEE Trans. Syst. Sci. Cyber. **5**(4), 322–333 (1969).
[22]S. Hochreiter and J. Schmidhuber, "Long short-term memory," Neural Comput. **9**(8), 1735–1780 (1997).
[23]A. Ng, "Cs229 course notes: Deep learning," Stanford Univ., Stanford, CA, USA, Tech. Rep., 2018.
[24]C. Rudin, "Stop explaining black box machine learning models for high stakes decisions and use interpretable models instead," Nat. Mach. Intell. **1**(5), 206–215 (2019).
[25]G. E. Karniadakis, I. G. Kevrekidis, L. Lu, P. Perdikaris, S. Wang, and L. Yang, "Physics-informed machine learning," Nat. Rev. Phys. **3**(6), 422–440 (2021).
[26]M. Raissi, P. Perdikaris, and G. Karniadakis, "Physics-informed neural networks: A deep learning framework for solving forward and inverse problems involving nonlinear partial differential equations," J. Comput. Phys. **378**, 686–707 (2019).
[27]A. D. Jagtap, Z. Mao, N. Adams, and G. E. Karniadakis, "Physics-informed neural networks for inverse problems in supersonic flows," J. Comput. Phys. **466**, 111402 (2022).

[28]A. D. Jagtap, E. Kharazmi, and G. E. Karniadakis, "Conservative physics-informed neural networks on discrete domains for conservation laws: Applications to forward and inverse problems," Comput. Methods Appl. Mech. Eng. **365**, 113028 (2020).
[29]A. Jagtap and G. Karniadakis, "Extended physics-informed neural networks (XPINNS): A generalized space-time domain decomposition based deep learning framework for nonlinear partial differential equations," Comm. Comput. Phys. **28**, 2002–2041 (2020).
[30]E. Kharazmi, Z. Zhang, and G. E. Karniadakis, "HP-VPINNS: Variational physics-informed neural networks with domain decomposition," Comput. Methods Appl. Mech. Eng. **374**, 113547 (2021).
[31]K. Li, K. Tang, T. Wu, and Q. Liao, "D3M: A deep domain decomposition method for partial differential equations," IEEE Access **8**, 5283–5294 (2020).
[32]M. F. Fathi, I. Perez-Raya, A. Baghaie, P. Berg, G. Janiga, A. Arzani, and R. M. D'Souza, "Super-resolution and denoising of 4d-flow MRI using physics-informed deep neural nets," Comput. Methods Programs Biomed. **197**, 105729 (2020).
[33]A. Arzani, J.-X. Wang, and R. M. D'Souza, "Uncovering near-wall blood flow from sparse data with physics-informed neural networks," Phys. Fluids **33**(7), 071905 (2021).
[34]R. Laubscher and P. Rousseau, "Application of a mixed variable physics-informed neural network to solve the incompressible steady-state and transient mass, momentum, and energy conservation equations for flow over in-line heated tubes," Appl. Soft Comput. **114**, 108050 (2022).
[35]C. Rao, H. Sun, and Y. Liu, "Physics-informed deep learning for incompressible laminar flows," Theor. Appl. Mech. Lett. **10**(3), 207–212 (2020).
[36]H. Eivazi, M. Tahani, P. Schlatter, and R. Vinuesa, "Physics-informed neural networks for solving Reynolds-averaged Navier–Stokes equations," Phys. Fluids **34**(7), 075117 (2022).
[37]M.-J. Xiao, T.-C. Yu, Y.-S. Zhang, and H. Yong, "Physics-informed neural networks for the Reynolds-averaged Navier–Stokes modeling of Rayleigh–Taylor turbulent mixing," Comput. Fluids **266**, 106025 (2023).
[38]E. J. Parish and K. Duraisamy, "A dynamic subgrid scale model for large eddy simulations based on the Mori–Zwanzig formalism," J. Comput. Phys. **349**, 154–175 (2017).
[39]Z. Li, T. Liu, W. Peng, Z. Yuan, and J. Wang, "A transformer-based neural operator for large-eddy simulation of turbulence," Phys. Fluids **36**(6), 065167 (2024).
[40]S. Shah and N. K. Anand, "Physics-informed neural networks for periodic flows," Phys. Fluids **36**(7), 073620 (2024).
[41]K. Hornik, M. Stinchcombe, and H. White, "Multilayer feedforward networks are universal approximators," Neural Netw. **2**(5), 359–366 (1989).
[42]R. Vinuesa and S. L. Brunton, "Enhancing computational fluid dynamics with machine learning," Nat. Comput. Sci. **2**(6), 358–366 (2022).
[43]M. Nielsen, *Neural Networks and Deep Learning* (Determination Press, 2015).
[44]A. Paszke, S. Gross, F. Massa, A. Lerer, J. Bradbury, G. Chanan, T. Killeen, Z. Lin, N. Gimelshein, L. Antiga *et al.*, "Pytorch: An imperative style, high-performance deep learning library," Adv. Neural Inform. Process. Syst. **32**, 8026–8037 (2019).
[45]P. K. Diederik, "Adam: A method for stochastic optimization," arXiv:1412.6980 (2014).
[46]X. Glorot and Y. Bengio, "Understanding the difficulty of training deep feedforward neural networks," in Proceedings of the Thirteenth International Conference on Artificial Intelligence and Statistics. *JMLR Workshop and Conference Proceedings* (PMLR, 2010), pp. 249–256.
[47]C. Song and R. Kawai, "Monte Carlo and variance reduction methods for structural reliability analysis: A comprehensive review," Probab. Eng. Mech. **73**, 103479 (2023).
[48]A. Villié, S. Schmitter, J. G. R. von Saldern, S. Demange, and K. Oberleithner, "Physics-informed neural networks for enhancing medical flow magnetic resonance imaging: Artifact correction and mean pressure and Reynolds stresses assimilation," Phys. Fluids **37**(2), 025194 (2025).
[49]U. Ghia, K. Ghia, and C. Shin, "High-Re solutions for incompressible flow using the Navier-Stokes equations and a multigrid method," J. Comput. Phys. **48**(3), 387–411 (1982).
[50]S. Kotian, N. Methekar, and S. Nikam, "A computational study of the influence of wavy arteries and veins on hemodynamic characteristics in an unsteady state," Phys. Fluids **36**(10), 101912 (2024).
[51]H. Lei, D. A. Fedosov, B. Caswell, and G. E. Karniadakis, "Blood flow in small tubes: Quantifying the transition to the non-continuum regime," J. Fluid Mech. **722**, 214–239 (2013).
[52]N. K. A. H. M. S. Bahaidarah and H. C. Chen, "Numerical study of heat and momentum transfer in channels with wavy walls," Numer. Heat Transf. A: Appl. **47**(5), 417–439 (2005).
[53]B. Ničeno and E. Nobile, "Numerical analysis of fluid flow and heat transfer in periodic wavy channels," Int. J. Heat Fluid Flow **22**(2), 156–167 (2001).